High-strength ultrafine-grained CoCrFeNiNb high-entropy alloy prepared by mechanical alloying: Properties and strengthening mechanism

High-strength ultrafine-grained CoCrFeNiNb high-entropy alloy prepared by mechanical alloying: properties and strengthening mechanism

Filip Průša*[1], Alexandra Šenková[1], Marcello Cabibbo[2], Andrea Školáková[1], Vojtěch Kučera[1], Zbyněk Veselka[1], Dalibor Vojtěch[1], Jaroslav Čapek[3]

[1]University of Chemistry and Technology, Prague, Department of Metals and Corrosion Engineering, Technická 5, 166 28 Prague 6, Czech Republic

[2]DIISM / Università Politecnica delle Marche, Via Brecce Bianche 12, I-60131 Ancona, Italy

[3]Institute of Physics of the CAS, Na Slovance 2, 182 21 Prague 8, Czech Republic

*Corresponding author: E-mail: prusaf@vscht.cz, tel.: +420220444441

Declaration of interest: none.

Abstract

An equiatomic CoCrFeNiNb alloy was prepared by conventional induction melting and by 8 h of mechanical alloying and compaction via spark plasma sintering. The alloy prepared via mechanical alloying showed a uniform ultrafine-grained microstructure composed of an FCC solid solution strengthened by HCP Laves phases. A detailed TEM inspection revealed the presence of nanocrystalline Cr_2O_3 particles at the triple junctions of the present grains as well as stacking faults and deformation nanotwins found exclusively in the interior of the FCC solid solution grains. The as-cast alloy had a high initial hardness of 648 ± 18 HV 30 and UCS of 1374 MPa and was outperformed by the mechanically alloyed alloy compacted at 1000 °C. The last mentioned alloy also showed an even higher hardness of 798 ± 9 HV 30 as well as an ultra-high UCS that reached 2412 MPa. Based on the TEM quantitative analyses considering the contributions of different structural constituents and lattice defects, the aforementioned UCS value was found to be in good agreement with results from microstructure strengthening modelling, which indicated a calculated mean value of 2300 ± 300 MPa. Moreover, the mechanically alloyed alloy also showed exceptional thermal stability even after long-term

annealing/testing at 600 °C because it maintained a hardness of 777 ± 5 HV 30, and the UCS still had an extraordinary value of 2284 MPa.

Keywords: Mechanical alloying; Strengthening mechanism; Transmission electron microscopy; Mechanical properties; Spark plasma sintering.

1. Introduction

High-entropy alloys (HEAs) belong to the group of modern and perspective materials that have been intensively studied since 2004, when Cantor et al. reported the first CoCrNiFeMn high-entropy alloy [1]. HEAs generally consist of five or more principal metallic elements whose chemical composition varies from 5 to 35 at. % [2-7], although in the past, the boundaries were believed to correspond precisely to an equiatomic composition made of five elements. These groups of alloys gained attention mostly due to their unique combination of properties, such as high strength [4, 8], high toughness together with high plasticity [9], high hardness [2, 3], excellent thermal stability [2], and promising wear [6] and corrosion resistance [10, 11]. Such unique properties are directly associated with the four principal core effects that include a high configurational entropy of mixing, sluggish diffusion, severe lattice distortion and the cocktail effect [12, 13]. A high configurational entropy of mixing affects the preferential formation of a solid-solution, which is more stable than intermetallic compounds, resulting in improved mechanical properties [10]. Although the single-phase solid solutions of HEAs offer an appropriate combination of desirable properties, secondary phase strengthening is currently of interest [14, 15]. Thus, considering all the above-mentioned properties, high-entropy alloys composed of solid solutions and secondary phases might find utilization in a wide range of applications mostly focused on construction materials, although the successful use of HEAs as a sintering aid for B_4C ceramics [3] or as binder for WC composites [16] has already been reported.

The chemical composition of the studied HEAs affects the obtained microstructure, phase composition and mechanical properties. HEAs may occur in face-centred cubic (FCC) single-phase (e.g., CoCrCuNiFe and CoCrMnFeNi), body-centred cubic (BCC) single-phase (e.g., CoCrNiFeNiAl, NbMoTaW and NbMoTaWV) or hexagonal close-packed (HCP) single-phase (e.g.,

GdDyErHoTb and GdErHoTb) materials [17]. It was shown that the FCC structure has good ductility and poor strength [6, 13, 18-21], while HEAs with a BCC structure exhibit excellent strength but reduced plasticity [9, 12, 22]. For this reason, it is necessary to find a balance to obtain an alloy with high strength and good ductility. One of the possibilities for improving ductility and preserving high strength concurrently is alloying with niobium. The radius of Nb is larger than the rest of the elements, and thus niobium causes severe lattice distortion, which can lead to greater strengthening in an alloy with an FCC structure [9, 23].

Moreover, the Nb has very negative enthalpies of mixing with Co, Fe, Cr and Ni [23, 24] and forms Nb-enriched Laves phases [25] with an HCP structure that are known to substantially increase the yield and fracture strength as well as the elastic modulus upon precipitating in an FCC matrix [10, 24-26]. The amount of Laves phases increases with increasing content of niobium in an alloy [10, 26]. Niobium also promotes a change in the microstructure to a eutectic structure, which exhibits excellent mechanical properties [2, 9, 10, 23, 25, 27]. However, plasticity decreases with an increasing volume fraction of Laves phases [25, 27]. Studies [3, 28] showed that a balanced content of Nb increases strength while maintaining sufficient ductility.

HEAs are prepared mostly by conventional induction melting [29-31], arc melting [2, 6-8, 10, 25, 26, 28, 32-39], although the growing interest in the powder metallurgy techniques including gas atomization [3] or mechanical alloying [13, 16-20, 22, 40-47], all of which are capable of refining the microstructure significantly, is seen in the recent research. In addition to commonly utilized arc melting, HEAs are usually produced by the combination of mechanical alloying (MA) and a suitable consolidation process to achieve maximized properties that could not be obtained by any other conventional method [4, 10, 13, 16-20, 22, 29, 31, 40-42, 44, 46, 47]. The main advantage of MA is an increased solubility of even immiscible elements, further supporting the creation of solid solutions in systems with a high configurational entropy [40]. For compaction, spark plasma sintering (SPS) is the most commonly used consolidation technique. The mechanical properties of alloys prepared by a combination of MA and SPS are significantly better than those of as-cast alloys because of the formation of a refined microstructure with nanocrystalline dimensions [19, 40]. The SPS

compaction process suppresses grain coarsening effectively and produces compact HEAs with extraordinary properties that are not comparable to those of as-cast alloys.

In this work, high-entropy equiatomic CoCrNiFeNb alloys were prepared by a combination of short-term (8 h) MA followed by compaction via SPS. The microstructure and mechanical properties of the alloys were compared to those of an identical alloy prepared by induction melting. The results showed that alloy prepared by a combination of MA+SPS showed an ultrafine-grained microstructure composed of an FCC solid solution strengthened by HCP Laves phases as well by Cr_2O_3 nanocrystalline particles. This resulted in excellent mechanical properties that outperformed the properties of the as-cast counterpart and were retained even when the material was exposed to elevated temperatures of 400 °C and 600 °C. The results were compared with the calculated contributions of each structural components towards the strengthening of the alloys based on the TEM observations.

2. Materials and methods

The equiatomic CoCrNiFeNb alloy was prepared by mixing the pure powders in corresponding ratios and forming a 20 g powder batch that was homogenized for at least 5 min. The powder mixture was placed into the milling mould together with milling balls made of AISI 420 stainless steel. The deleterious cold welding was partially suppressed by the addition of 5 wt.% of n-heptane as a process control agent (PCA). The mould was sealed and flushed with argon (purity of 99.996%) for at least 3 min with a flow rate of 2 $l \cdot min^{-1}$. The mechanical alloying (MA, Retsch PM100, Haan, Germany) was performed at a speed of 400 rpm in 30 min intervals followed by 10 min breaks to allow the alloys to cool. These steps were repeated until the mechanical alloying process itself reached 8 h.

The prepared powder alloys were compacted by a spark plasma sintering device (SPS, FCT Systeme HP D 10, Frankenblicke, Germany) using a die, pistons and sealing papers all made of graphite. Prior to compaction, differential thermal analysis (DTA, DT-TGA Setys Evolution, Setaram France) of the prepared CoCrFeNiNb powder alloy was done in an Al_2O_3 crucible under an Ar atmosphere with a heating rate of 10 $°C \cdot min^{-1}$ to a final temperature of 1200 °C. Based on the results obtained by the DTA, the influence of two compaction temperatures, 800 °C and 1000 °C, was tested. The heating rate of the compaction processes was set to

200 °C·min^{-1} regardless of the final compaction temperature, while the samples were heated up to compaction temperature and then compressed by a pressure of 48 MPa. The samples remained at the compaction temperature 10 min to suppress the deleterious microstructural coarsening. Afterwards, the samples were cooled with the maximum cooling speed on the SPS device until they reached laboratory temperature. The prepared compact samples were circular in shape with a total thickness of approximately 4 mm and diameter of 20 mm.

The MA+SPS compacts were ground using diamond grinding plates marked as P120 – P1000, polished with diamond paste and etched in a mixture of HNO_3 and HCl (ratio of 1:3). The microstructure was observed using light microscopy (LM, Olympus PME-3) and scanning electron microscopy (SEM, Tescan LYRA, 20 kV, BSE+SE detectors) equipped with energy dispersive spectroscopy (EDS, Oxford Instruments, 80 mm^2).

Phase identification and quantitative microstructure strengthening evaluation were carried out by transmission electron microscopy (TEM, Philips™ CM-200®) equipped with a double-tilt specimen holder and a liquid N_2 cooling stage with a working voltage of 200 keV. TEM samples were prepared by grinding, polishing and dimpling 3 mm discs. The final preparation for electron transparency was carried out in a precision-ion milling system (PIPS, Gatan™) in a vacuum at a voltage of 12 V and with a tilting incident angle of 8° for the first half, 6° for the following quarter, and 4° for the final quarter of the whole Ar-ion thinning time. The statistical data were obtained by 3 different TEM discs. TEM analysis was carried out on the MA+SPS at 1000 °C compacted CoCrFeNiNb equiatomic alloy. All statistical evaluations of the microstructure features were carried out by stereological methods according to EN-112.

The phase and chemical composition were determined using X-ray diffraction (XRD, PANalytical X'Pert PRO, Netherlands, Cu Kα = 1.54059·10^{-10} m) and X-ray fluorescence (XRF, PANalytical, Netherlands). The surface porosity of the compact samples was measured by the threshold method using ImageJ software.

The mechanical properties of the prepared compact samples were measured by Vickers hardness tests and by compressive stress-strain tests done at the laboratory and elevated temperatures. For the hardness testing, a load of 30 kg with a dwell time of 10 s was used until at least 10 indents were measured. For the compressive stress-strain tests, rectangular specimens were cut using a diamond blade (Leco VariCut VC-50) with a height that was 1.5

times the length of the side. The compressive tests were done on a universal testing machine (Labortech, LabTest SP 250.1-VM) with a strain speed of 0.001 s^{-1} using at least three samples, while the temperature during the tests was 25 °C, 400 °C and 600 °C. Since we presumed that the tested alloys would exhibit excellent thermal stability at elevated temperatures, the samples were placed between two ceramic plates made of Al_2O_3. The compact samples were also tested for thermal stability expressed as a hardness change during long-term annealing at 400 °C and 600 °C, while the hardness change was measured after 1, 4, 9, 25, 50, 75 and 100 h of annealing. To fully explore the thermal stability of the MA+SPS alloys, the prepared rectangular samples were annealed under the same conditions and compression tested at 25 °C.

To compare the properties of the prepared alloys, an identical alloy was prepared using induction melting. The appropriate amounts of each element were placed into the Al_2O_3 crucible and melted under an argon protective atmosphere at a temperature of approximately 1800 °C. The melt was then homogenized through eddy currents for several minutes and poured into a steel mould to form an ingot 14 mm in diameter and with a total length of almost 150 mm.

3. Results and discussion

3.1 Chemical composition of alloys

The above-mentioned equiatomic alloy was prepared using either conventional induction melting or mechanical alloying. The results corresponding to the changes in chemical composition determined by the XRF analysis are shown in Fig. 1. As is evident, the chemical composition of the as-cast alloy was around the intended 20 at.%, except for the slightly higher content of Ni and lower content of Nb. The lower content of Nb might be attributed to the highest melting temperature of the Nb (2477 °C) among all the elements used. However, this presumption has not been confirmed since there were no traces of non-melted Nb particles suggesting partial pre-oxidization of the Nb.

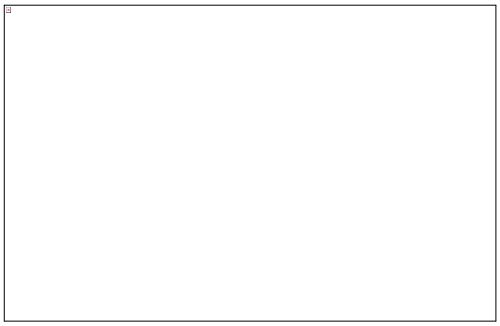

Fig. 1: The chemical composition of the prepared CoCrFeNiNb alloys determined by XRF. *(Different durations of the MA process are displayed.)*

The Gibbs free energy was calculated using FactSage software (see Tab. 1) for the formation of the most common oxide products, and it reached a minimum value for Nb_2O_5. Since the induction melting was done in an Ar protective atmosphere, the oxidation during the melting was completely excluded from consideration as one of the very few likely causes. The main reason the content of Nb was decreased in the as-cast alloy can be attributed to the partial pre-oxidation of the Nb chunks that reduced the overall concentration of Nb in the alloy, which is reasonable considering the very high melting temperature of Nb and its high affinity for O_2.

In comparison, the alloys prepared using MA (see Fig. 1) showed a steep increase in the Fe content due to the formation of hard and therefore highly abrasive phases through the 8 h of the MA process. Due to the XRD results, the 8 h MA was determined to be sufficient to prepare a nearly equiatomic FCC solid solution alloy strengthened by a Laves phase; thus, increased MA times were not used.

Tab. 1: Calculated values of the Gibbs free energy corresponding to the formation of the most common oxides at a temperature of 298.16 K.

Reaction	**Compound**	$-\Delta G^{\circ}_{298.16}\ [kJ \cdot mol^{-1}]$
$2Co + O_2 \rightarrow 2CoO$	CoO	-214.02
$4Cr + 3O_2 \rightarrow 2Cr_2O_3$	Cr_2O_3	-1046.69
$4Fe + 3O_2 \rightarrow 2Fe_2O_3$	Fe_2O_3	-744.02
$2Fe + O_2 \rightarrow 2FeO$	FeO	-244.88
$2Ni + O_2 \rightarrow 2NiO$	NiO	-211.76
$4Nb + 5O_2 \rightarrow 2Nb_2O_5$	Nb_2O_5	-1765.97

(Values were calculated using FactSage software.)

3.2 DTA results

To determine the best compaction temperature for the SPS and describe the processes that occur during heating of the mechanically alloyed powders, DTA was done, as shown in Fig. 2. The sample demonstrated exothermic behaviour up to a temperature of approximately 700 °C that corresponds to a partial relaxation of the lattice stress-strain imposed during MA. At 700 °C, very slow grain growth started reaching a plateau at 800 °C and then progressed more quickly, which resulted in endothermic behaviour as the temperature increased. Another important finding is that the prepared powders of nearly equiatomic CoCrFeNiNb alloy did not melt in at the tested temperatures, suggesting a possible temperature range for the subsequent compaction via SPS. Although we did not observe melting of the sample, Jiang et al. [35] reported a melting temperature of 1251 °C for the eutectic $CoCrFeNiNb_{0.45}$ alloy. Thus, the first temperature for the compaction was chosen to be 800 °C to suppress the microstructural coarsening, while the higher temperature of 1000 °C was expected to provide better particle-to-particle cohesion at the expense of microstructural coarsening.

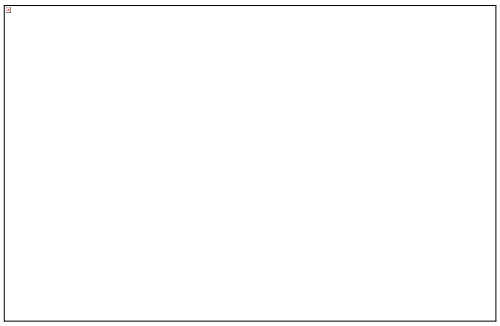

Fig. 2: The results of DTA for the mechanically alloyed CoCrFeNiNb powder alloy.

3.3 Microstructure and phase composition of compacts

The LM micrographs of both the MA+SPS alloys and the as-cast alloy are shown in Fig. 4. The microstructure reflects that the preparation processes were entirely different, and the as-cast alloy had a coarser microstructure than the ultrafine-grained alloy prepared by MA+SPS. The microstructure of the as-cast alloy (Fig. 3a) shows the presence of primary dendrites surrounded by eutectic-like structures that are visible even without etching. In the as-cast alloy,

pores are also visible, reaching an average 0.61 ± 0.07% (see **Errore. L'origine riferimento non è stata trovata.**). On the other hand, both the MA+SPS alloys (Fig. 3b and c) show a uniform, well-refined microstructure with structural constituents that are hardly distinguishable with LM but can be sufficiently displayed using SEM/TEM techniques. Among the well-refined microstructures, the MA+SPS alloys had a different level of porosity, reaching up to approximately 24.75 ± 4.49% (**Errore. L'origine riferimento non è stata trovata.**) for the MA+SPS alloy compacted at 800 °C. Since the porosity of the alloy compacted at 800 °C was too high, the MA powders were compacted at higher temperatures to effectively eliminate the porosity. Thus, an increase in the SPS compaction temperature to 1000 °C decreased the porosity to 0.23 ± 0.14% (Fig. 3c, **Errore. L'origine riferimento non è stata trovata.**), a value even below the as-cast counterpart.

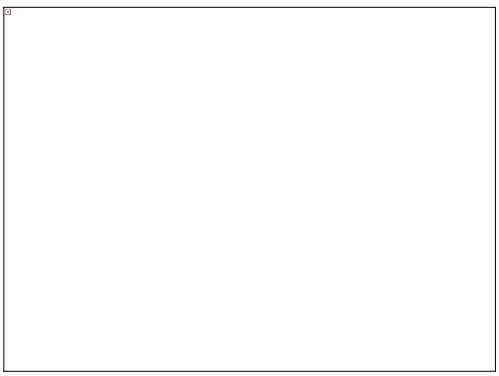

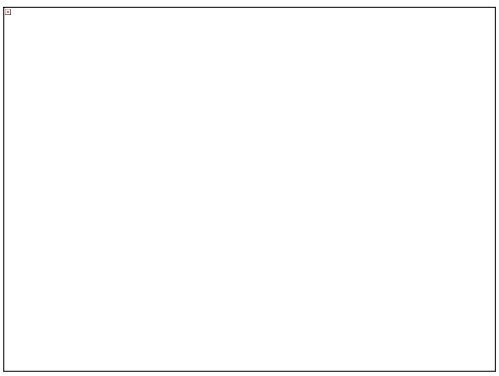

Fig. 3: The LM micrographs of the equiatomic CoCrFeNiNb alloy prepared by: a) induction casting; b) 8 h MA+SPS at 800 °C; c) 8 h MA+SPS at 1000 °C. *(All micrographs were taken prior etching.)*

It is evident that the higher temperature of 1000 °C allowed better particle-to-particle cohesion due to thermal activation of non-discrete dislocation movements and successfully reducing the level of deleterious porosity. The remaining pores were circular in shape, while their distribution was completely random in the MA+SPS alloy compact.

Tab. 2: The average surface porosity of the equiatomic CoCrFeNiNb alloys prepared by different techniques along with confidence intervals.

CoCrFeNiNb (preparation)	**Porosity [%]**
As-cast	0.61 ± 0.07
8h MA+SPS at 800 °C	24.75 ± 4.49
8h MA+SPS at 1000 °C	0.23 ± 0.14

The more detailed SEM micrographs of the as-cast alloy and both of the MA+SPS alloys are shown in Fig. 4. Since the as-cast alloy reference was prepared using conventional induction melting, the microstructure showed the presence of primary dendrites surrounded by eutectic-like structures (Fig. 4a). On the other hand, both of the MA+SPS alloys showed a refined microstructure (Fig. 4b and c) with no traces of the structures found in the as-cast alloy. The present phases were refined to sub-micrometre dimensions and showed a uniform distribution within the sample regardless of the SPS compaction temperature. In addition, the MA+SPS alloy compacted at a temperature of 1000 °C showed a significant reduction in the porosity and had a slightly coarser microstructure compared to that compacted at 800 °C (compare Fig. 4b and c).

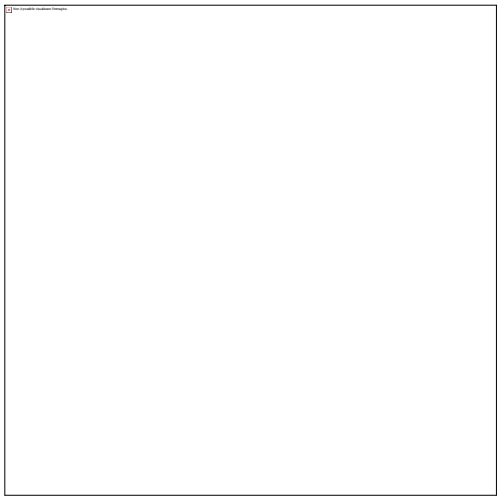

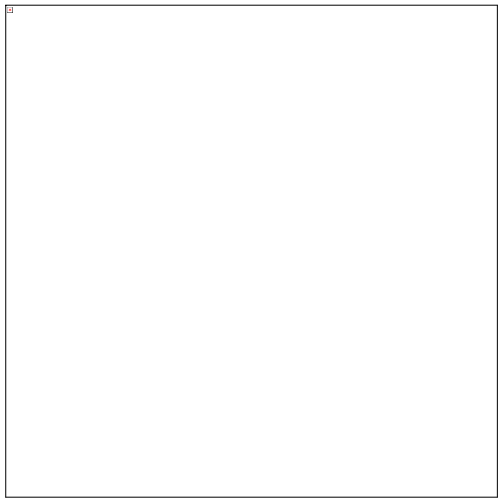

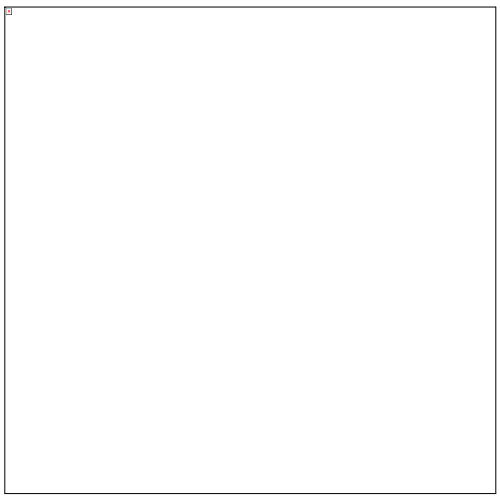

Fig. 4: The SEM micrographs of the equiatomic CoCrNiFeNb alloy prepared by: a) induction melting; b) MA+SPS at 800 °C; c) MA+SPS at 1000 °C. *(images were taken using 80% of BSE and 20% of SE detectors)*

The phases were determined using X-ray diffraction, and the results are shown in Fig. 5. As the initial powders were mixed and homogenized for a sufficient time, the reflections corresponding to pure elements are distinguishable. The first 4 h of MA resulted in a reduction in the characteristic patterns of pure elements and increase in the reflections by a newly formed solid solution with an FCC crystallographic lattice and a small amount of HCP Laves phase. Thus, this observation does not correspond with the findings by Vaidya et al. [4], who suggested the formation of only metastable solid solutions that then exhibit phase transformations during compaction. Furthermore, the phase composition of the MA powders and MA+SPS alloys also corresponds to the calculated pseudobinary phase diagram for CoCrFeNi-Nb [9] that predicted and confirmed the presence of an FCC solid solution strengthened by the HCP Laves phase. However, the preparation technique combines severe plastic deformation and fragmentation of the powders, so the precise identification of present

phases was quite challenging with XRD. Additionally, the mutual element substitution in the crystallographic lattice shall be considered.

Fig. 5: XRD diffraction patterns of the equiatomic CoCrFeNiNb alloys showing the results for the powder mixture, powder alloys and MA+SPS alloys compacted at 800 °C and 1000 °C.

Furthermore, a prolonged MA of up to 8 h resulted in the formation of an increased volume fraction of HCP Laves phases, increasing the intensity of the corresponding peaks. Peak broadening was also observed, suggesting either microstructural refinement or an increase in the lattice stress-strain due to the nature of the chosen processing method. Consequently, the prepared powder samples were compacted using the SPS method at the two temperatures of 800 and 1000 °C, which did not change the phase composition, although it reduced the stress-strain within the crystallographic lattices of the present phases and caused microstructural coarsening. This effect was even much more evident for the MA+SPS alloy compacted at a temperature of 1000 °C than that at 800 °C.

On the other hand, the as-cast alloy also showed the presence of an FCC solid solution and Laves phases, although the corresponding reflections were narrow. These results corresponded to the previously observed micrographs (see Fig. 3 and Fig. 4) that show the presence of either large structural constituents, in the case of as-cast alloy, or refined microstructures containing a sub-micrometre constituent, as in the case of the MA+SPS alloys.

In comparison, the as-cast alloys showed rather narrow peaks corresponding also to an FCC solid solution as well to the presence of HCP Laves phases. Thus, the phase composition was identical to that of MA+SPS alloys and corresponded to the findings of others [30] who observed the same phase composition even when prepared by different techniques and slightly different chemical compositions. The results of the XRD analysis demonstrate the ability of our approach to prepare the HEAs with the targeted phase compositions within the time of several hours of the MA process. It should be noted that similar results have not been reported for rapid MA suitable for the production of HEAs, with the exception of our previous research [19]; the results reported herein are comparable to the data reported by others [13, 16-18, 20, 22, 40-42] who prepared the HEAs via a MA process significantly longer than 8 h.

The SEM+EDS element distribution maps of the as-cast and both MA+SPS alloys are shown in Fig. 6. As shown, the as-cast alloy (Fig. 6a) showed the presence of two different types of structural constituents consisting of primary dendrites and eutectic-like structures, which were distinguished from each other by different contents of Cr, Fe, Ni and Nb. The primary dendrites were mainly enriched with Nb, while the interdendritic eutectic-like region showed the presence of dark-grey phases containing mainly Cr, Fe and Ni and bright phases containing mainly Nb. In addition, the Co content was homogeneously distributed between all the observed structural components. The same element distribution between the structural constituents has already been observed by Tsai et al. [38], who identified them as Nb-rich dendrite-like phases, while the interdendritic structures were identified as a mixture of HCP C14 Laves phases (bright needle-like structures) and an FCC solid solution (dark grey).

Compared to that the results above, both the MA+SPS alloys (Fig. 6b and c) showed a significantly refined microstructure composed of phases with dimensions in a range of several tens of nanometres, which was primarily found for the MA+SPS alloy compacted via SPS at 800 °C. It should be noted that the dimensions of the present phases in this particular compact alloy were far below the detection limit of EDS (Fig. 6b). Although the microstructure showed the presence of ultrafine-grained phases, the MA+SPS alloy compacted at 800 °C showed enormous residual porosity and rather low particle-to-particle cohesion, which substantially degraded the mechanical properties. However, the compaction at a higher temperature of 1000 °C resulted in microstructure coarsening that increased the dimensions of the present

phases up to 300 nm (Fig. 6c). The overall porosity (see **Errore. L'origine riferimento non è stata trovata.**) was lower although the coarser microstructure allowed formation of small dimples due to a localized dissolution of the alloy in the presence of Cl^- ions. Considering the significant difference in the microstructures, a much more suitable compaction technique using ultra-high pressures in a range of several GPa might overcome this disadvantage, yielding results that are superior to those shown below.

Fig. 6: The SEM+EDS element distribution maps of the CoCrFeNiNb alloy prepared by: a) induction melting; b) 8 h MA+SPS at 800 °C; c) 8 h MA+SPS at 1000 °C. *(images were taken using 80% of BSE and 20% of SE detectors)*

The individual structural components in the as-cast and MA+SPS alloys were also investigated using SEM+EDS point analysis (see Fig. 7), and the results are shown in

CoCrFeNiNb (preparation)	Points	Average chemical compositon [at.%]					Corresponding phase
		Co	Cr	Fe	Ni	Nb	
as-cast	1-4	20±0.2	21.95±0.4	20.3±0.2	22.1±0.3	15.7±0.7	HCP Laves phase
	5-8	19.5±0.2	25.5±0.4	22.7±0.5	24.9±0.6	7.4±1.1	FCC
	9-12	20.9±0.2	17.9±0.2	19.3±0.1	15.7±0.9	26.3±0.8	HCP Laves phase
8h MA+SPS at 800 °C	1-4	20.5±0.1	20.3±0.1	25.3±0.1	20.4±0.1	13.5±0.3	HCP Laves phase
	5-8	20.2±0.1	21.2±0.1	25.9±0.1	20.4±0.3	12.4±0.1	FCC
8h MA+SPS at 1000 °C	1-4	21.9±0.4	18.3±0.3	21.9±0.1	19.6±0.3	18.4±0.6	HCP Laves phase
	5-8	19.8±0.2	22.2±0.2	25.4±0.5	21.7±0.4	10.9±0.9	FCC

. In the as-cast alloy (Fig. 7a), the eutectic-like structures differed in the elemental contents, specifically in the Nb content, which was low in the dark-grey phases, while the bright phases showed an almost equiatomic content of Nb reaching up to average value of 15.7±0.7 at.%. The appearance of the structures is due to the imaging mechanism in the BSE detector, where an increasing atomic number causes the brightness of a structure in an image to increase. Based on that mechanism, the primary dendrites of the HCP Laves phase showed an increased content of Nb corresponding to 26.3±0.8 at.%, while the remaining elements were equal to 20 at.% or below. The chemical composition of the dendrites within the as-cast alloy is in good agreement with the work of Yu et al. [2], Tsai et al. [38] and Jiang et al. [26, 35], who reported a similar chemical composition with a concentration of Nb ranging between 26.7 and 31.8 at.%. However, none of the authors reported the exact chemical composition of the eutectic-like structures at the level of each structural constituent.

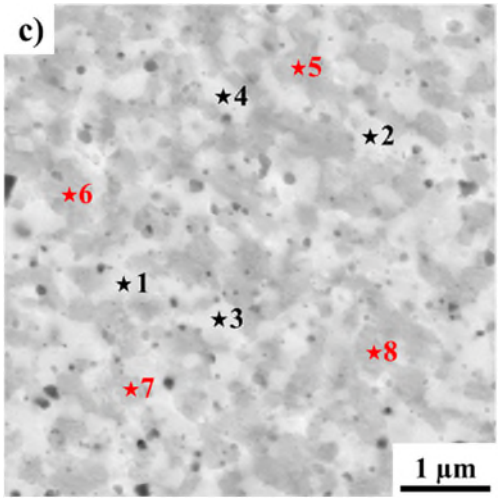

Fig. 7: The SEM micrographs with points marked for EDS analysis of the: a) as-cast; b) MA+SPS at 800 °C; c) MA+SPS at 1000 °C alloys.

On the other hand, the MA+SPS alloy (Fig. 7b) compacted at 800 °C showed an ultrafine-grained microstructure composed of phases whose chemical composition was hardly distinguishable due to the physical limitations of the 80 mm^2 EDS detector. Based on the micrographs and the physical aspects of used detectors, the microstructure more or less showed the presence of two phases, one of which contained more Nb (bright phase), while the second contained less Nb. In contrast, the compaction at a higher temperature of 1000 °C caused microstructural coarsening (Fig. 7c); bright phases with nearly equiatomic compositions were present, while the dark phases contained a decreased amount of Nb of approximately 10 at.%. In addition, the presence of dark spots was also observed, and their presence arose during etching as a consequence of Cl^- ions in the etching solution, which caused localized dissolution forming dimples. Considering the results mentioned above, the

combination of MA+SPS resulted in significant microstructural refinement and a nearly equiatomic chemical composition within the bright phases. On the other hand, the dark phases in the MA+SPS alloys were supersaturated with up to 26.0 at.% Fe.

Tab. 3: Results of the SEM+EDS analysis (in at.%) of points marked in Fig. 7.

CoCrFeNiNb (preparation)	Points	Average chemical compositon [at.%]					Corresponding phase
		Co	Cr	Fe	Ni	Nb	
as-cast	1-4	20±0.2	21.95±0.4	20.3±0.2	22.1±0.3	15.7±0.7	HCP Laves phase
	5-8	19.5±0.2	25.5±0.4	22.7±0.5	24.9±0.6	7.4±1.1	FCC
	9-12	20.9±0.2	17.9±0.2	19.3±0.1	15.7±0.9	26.3±0.8	HCP Laves phase
8h MA+SPS at 800 °C	1-4	20.5±0.1	20.3±0.1	25.3±0.1	20.4±0.1	13.5±0.3	HCP Laves phase
	5-8	20.2±0.1	21.2±0.1	25.9±0.1	20.4±0.3	12.4±0.1	FCC
8h MA+SPS at 1000 °C	1-4	21.9±0.4	18.3±0.3	21.9±0.1	19.6±0.3	18.4±0.6	HCP Laves phase
	5-8	19.8±0.2	22.2±0.2	25.4±0.5	21.7±0.4	10.9±0.9	FCC

(Average chemical composition of points is shown together with standard deviation.)

The Fig. 8 shows a representative BF-TEM micrograph of the alloy compacted at 1000 °C in which the three different constituents can be easily recognized. The three phases were also crystallographically identified by means of selected area electron diffraction patterns (SAEDPs). These are shown in Fig. 8b. The CoCrFeNiNb equiatomic HEA consists of a FCC solid solution identified as γ type-like phase characterized by a diffuse presence of tangled dislocations and twinning, a hexagonal close-packed (HCP) Laves phase, and HCP Cr_2O_3 intergranular rounded oxides. The grains of the FCC phase showed the presence of lattice defects, mainly composed of dislocation pile-ups found in the solid solution, deformation nanotwins, and to some extent, the presence of secondary phase particles. The presence of stacking faults as well as nanotwins was also reported by He et al. [21], who prepared a $CoCrFeNiNb_{0.1}$ alloy by cryogenic rolling with a total thickness reduction of 50%. The presence of deformation twins in the HEAs has been reported by Rogal et al. [43] who prepared a CoCrFeNiMn high entropy alloy reinforced with SiC spherical nanoparticles. These nanocrystalline particles initially enabled the creation of deformation twins that supported their limited growth within the grain interiors and also acted as effective barriers.

The Laves lattice is a Co_2Nb-type structure, with crystallographic parameters a = 0.4835 nm and c = 0.7860 nm. Jiang et al. [26] reported the composition of this Laves phase as $Co(Ni,Fe,Cr)_2Nb$, while Liu et al. [48] reported a slightly different composition of

$(Co,Fe,Ni)_2(Cr,Nb)$. Both compositions refer to HCP Laves crystallographic structures. Thus, based on the EDS analyses reported in the

CoCrFeNiNb (preparation)	Points	Average chemical compositon [at.%]					Corresponding phase
		Co	Cr	Fe	Ni	Nb	
as-cast	1-4	20±0.2	21.95±0.4	20.3±0.2	22.1±0.3	15.7±0.7	HCP Laves phase
	5-8	19.5±0.2	25.5±0.4	22.7±0.5	24.9±0.6	7.4±1.1	FCC
	9-12	20.9±0.2	17.9±0.2	19.3±0.1	15.7±0.9	26.3±0.8	HCP Laves phase
8h MA+SPS at 800 °C	1-4	20.5±0.1	20.3±0.1	25.3±0.1	20.4±0.1	13.5±0.3	HCP Laves phase
	5-8	20.2±0.1	21.2±0.1	25.9±0.1	20.4±0.3	12.4±0.1	FCC
8h MA+SPS at 1000 °C	1-4	21.9±0.4	18.3±0.3	21.9±0.1	19.6±0.3	18.4±0.6	HCP Laves phase
	5-8	19.8±0.2	22.2±0.2	25.4±0.5	21.7±0.4	10.9±0.9	FCC

, a Laves composition of $(Co,Fe,Ni)_2(Cr,Nb)$ was suspected here. Between these two phases, at the triple grain junction, the presence of small rounded Cr_2O_3 oxides with an average diameter of 100 nm was observed. The volume fraction of these particles was below the detection limit of XRD and thus was not identified in the corresponding patterns (Fig. 5).

The microstructure strengthening of the three detected HEA constituents after 1000 °C SPS compaction conditions was calculated by the quantitative analyses of the TEM micrographs, as is shown in Section 3.5.

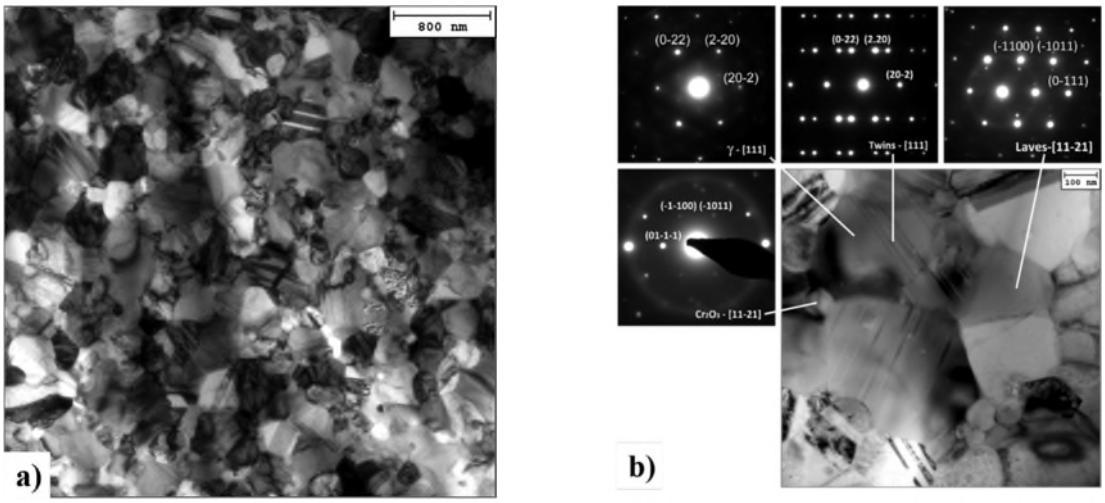

Fig. 8: BF-TEM micrographs of the 8 h MA+SPS alloy compacted at 1000 °C showing: a) a complex overview of the existing phases; b) details of the microstructure. *(SAEDPs refer to the FCC γ phase, the HCP Laves phase, the twinning inside the Laves phase, and the HCP Cr_2O_3 oxide particles.)*

1. Mechanical properties

The mechanical properties of either the as-cast alloy or the MA+SPS compacts were thoroughly investigated, and their results are summarized in **Errore. L'origine riferimento non è stata trovata.**. For this purpose, the hardness of the alloys was determined before any thermal treatment (Fig. 9). The induction melting resulted in a rather coarse microstructure, yielding a surprisingly high hardness of 648 ± 18 HV 30 due to a presence of large grains of HCP Laves phase. On the other hand, the combination of MA and subsequent compaction via SPS at 800 °C failed to deliver the expected results, negating its superiority over its as-cast counterpart. The main reason for the low hardness of only 93 ± 10 HV 30 was the poor or non-existent cohesion between the powder particles together with a high residual porosity that reached approximately up to 25%. Thus, the alloy compacted at 800 °C was not used for further investigation of the mechanical properties. However, increasing the compaction temperature up to 1000 °C tremendously reduced the porosity, and the compacts showed excellent particle-to-particle cohesion. Together with an ultrafine-grained microstructure, the hardness was 798 ± 9 HV 30, which was the highest value of all tested alloys. It should be noted that this value is superior to that reported by Yu et al. [2] (643 HV), which was obtained for a $CoCrFeNiNb_{0.8}$ alloy prepared by arc melting. Furthermore, the results of the investigated MA+SPS alloy is also superior to the results reported by Fang et al. [27], who prepared a plasma cladded $CoCrFeNiNb_x$ (x = 0.25) alloy that reached a hardness of approximately 525 HV. Moreover, Cheng et al. [41] prepared a senary CoCrFeNiMnAl1 (at.%) alloy via MA that was strengthened by different carbides as well by Al_2O_3 particles and reached a maximum hardness of 684 HV 1. However, it should be noted that the mentioned senary alloy was far more complex, and foremostly prepared by 45 h MA.

Tab. 4: The summary of mechanical properties of the equiatomic CoCrFeNiNb alloys.

CoCrFeNiNb (preparation)	**Test temperature [°C]**	**YCS [MPa]**	**UCS [MPa]**	**D [%]**	**HV 30**
As-cast	25	*	1374	*	648 ± 18
	400	*	1127	*	674 ± 4
	600	*	1280	*	676 ± 4
8h MA+SPS at 800 °C	25	*	351	*	93 ± 10
	400	-	-	-	-
	600	-	-	-	-

	25	*	2412	*	798 ± 9
8h MA+SPS at 1000 °C	400	*	2249	*	761 ± 7
	600	2178	2284	< 1	777 ± 5

(YCS – yield compressive strength in MPa; UCS – ultimate compressive strength in MPa; D – total plastic deformation in %; HV 30 – Vickers hardness measured with 30 kg which taken either prior or after 100 h annealing at corresponding temperature) **the values could not be determined due to brittle behaviour of the alloy*

Thus, the ultra-high hardness of the investigated MA+SPS alloy was achieved mainly due to an ultrafine-grained microstructure containing a high volume fraction of HCP Laves phases, which made a significant contribution to the overall hardness and strength, although it simultaneously reduced the ductility of the alloy [26]. On the other hand, the as-cast alloy showed a decreased, but still highly comparable, hardness of 648 ± 18 HV 30 mainly due to the coarse microstructure.

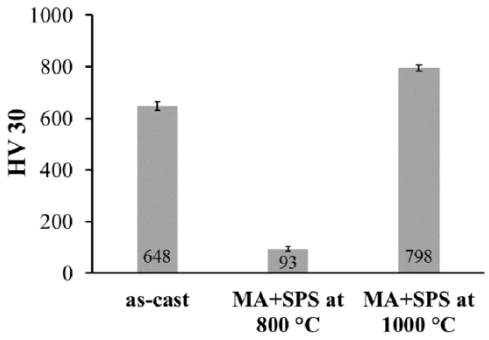

Fig. 9: Hardness of the as-cast and of the MA+SPS equiatomic CoCrFeNiNb alloys consolidated at different temperatures.

The results of the thermal stability of the alloys during long-term annealing at 400 °C and 600 °C are shown in Fig. 10. Both the as-cast and the MA+SPS (1000 °C) alloys showed an exceptional thermal stability that manifested as an almost negligible change in hardness even when the alloys were exposed to 100 h of annealing. In addition, both the as-cast and MA+SPS alloys showed a small decrease in the hardness in the first hours of annealing, followed by an immediate increase that was maintained until the end of the annealing at both 400 °C and 600 °C. The observed hardness decrease in both alloys during the first hours of annealing can

be attributed to a partial stress-strain relaxation of the crystallographic lattice. This presumption is further supported by the fact that the stress-strains should be considerably lower in the as-cast alloy since the only source of such lattice tensions originated due to thermally associated effects during rapid solidification. Thus, the hardness decrease in the as-cast alloy should be much lower than that in the MA+SPS alloys. On the other hand, the resulting hardness increase in both alloys might be associated with a change in the chemical compositions of each structural constituent, e.g., by increasing the volume fraction of the strengthening Laves phases. The hardness remained almost constant until the end of the annealing process, showing the excellent softening resistance of the CoCrNiFeNb alloys (see **Errore. L'origine riferimento non è stata trovata.**). The main reason for this excellent thermal stability was attributed to low inter-diffusion of the elements, which suppressed microstructural coarsening.

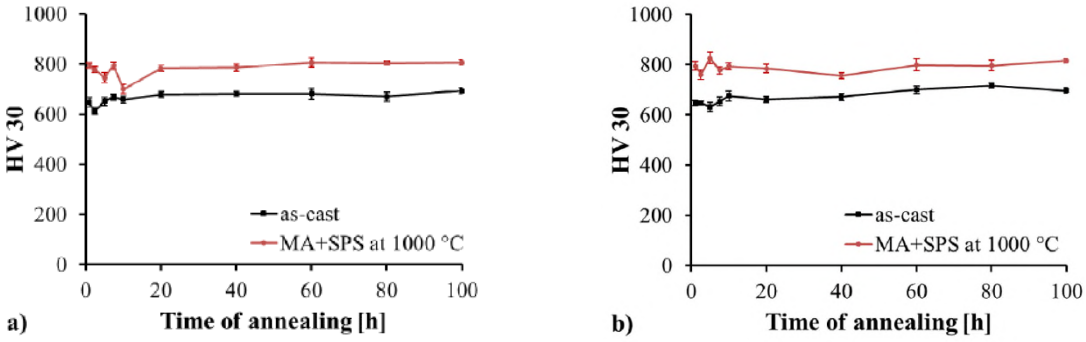

Fig. 10: The hardness change of the equiatomic CoCrFeNiNb alloys during long-term annealing at temperatures of: a) 400; b) 600 °C. *(error bars represent 95% confidence interval)*

The as-cast and MA+SPS alloys were also tested by a compressive stress-strain test, and the results are shown in Fig. 11. As shown in **Errore. L'origine riferimento non è stata trovata.**, the MA+SPS alloy compacted at 1000 °C showed the highest mechanical properties compared to the rest of the tested samples. In its initial state, it reached a UCS of 2412 MPa, while the as-cast alloy reached a UCS of only 1374 MPa. On the other hand, the MA+SPS alloy compacted at a temperature of 800 °C did not yield satisfactory results due to the previously mentioned

large residual porosity that reduced its UCS to only 351 MPa. Thus, the MA+SPS alloy compacted at 800 °C was not used for further testing.

The results of the investigated MA+SPS alloys were superior to those of others. For example, Qin et al. [25] observed a constant increase in the UCS with increasing Nb content for a similar $(CoCrCuFeNi)_{100-x}Nb_x$ (X=0-16) alloy prepared by arc melting, where a maximum value of 1322 MPa was reached and corresponded to the $(CoCrCuFeNi)_{84}Nb_{16}$ alloy. Moreover, the microstructure was composed of only an FCC solid solution up to a content of 8 at.% Nb; the Laves phase was created at higher Nb contents. Thus, the observed high values of the UCS of the investigated MA+SPS alloys were caused by solid solution strengthening due to the Nb atoms with a large diameter as well by the presence of Laves phases.

It should be noted that a simple substitution of Mn by Nb in the investigated MA+SPS alloys resulted in a tremendous increase in the compressive properties when compared to the results of our previous research that focused on equiatomic CoCrFeNiMn alloys [19]. The increase in the UCS of the MA+SPS alloy corresponds to a significant microstructural refinement that involved grain boundary strengthening, solid solution strengthening and strengthening via HCP Laves phases that were homogeneously distributed in the MA+SPS material. These observations are in good accordance with the reports of others [26, 48], who also reported strengthening of CoCrFeNiNb alloys via these three cooperating phenomena. Furthermore, the abovementioned strengthening factors were accompanied by dislocation strengthening and twinning strengthening mechanisms.

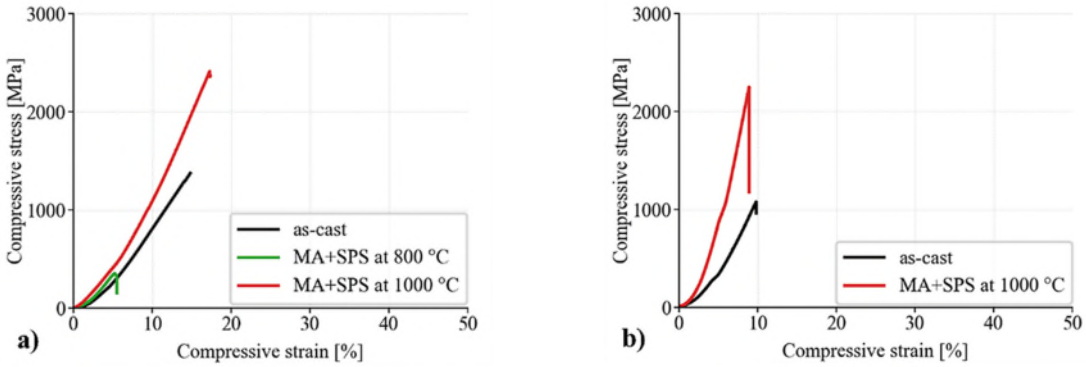

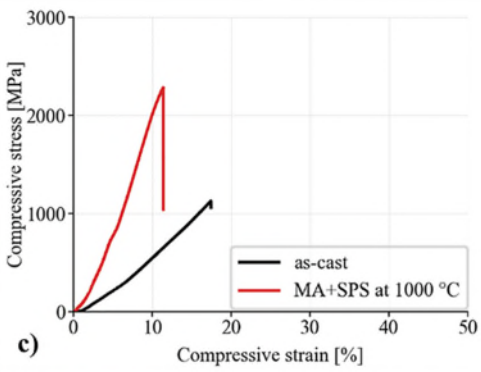

Fig. 11: The compressive stress-strain curves for the equiatomic CoCrFeNiNb alloy tested at: a) laboratory temperature; b) at 400 °C; c) at 600 °C.

During the tests at 400 °C (Fig. 11b), both alloys reduced their UCS, although the MA+SPS alloy had a UCS of 2249 MPa, a value twice as high as that of the as-cast alloy that reached a UCS of 1127 MPa. Furthermore, the compressive tests performed at a temperature of 600 °C (Fig. 11c) confirmed the exceptional thermal stability of both equiatomic CoCrFeNiNb alloys, showing identical or even slightly higher UCS compared to those obtained at 400 °C (Fig. 11b, **Errore. L'origine riferimento non è stata trovata.**). The as-cast alloy reached a UCS of 1280 MPa, while the MA+SPS alloy reached a UCS of 2284 MPa at 600 °C.

This behaviour of the MA+SPS alloy over the whole range of tested temperatures was caused by the ultrafine-grained microstructure that contained an FCC solid solution with grains below 200 nm as well by the presence of HCP Laves phases, which acted as significant strengthening elements. Moreover, the presence of Cr_2O_3 particles with dimensions of several tens of nm at triple junctions of the grains (Fig. 8b) contributed to the thermal stability of the MA+SPS alloy due to suppressing the grain growth during annealing. The Cr_2O_3 particles are thermally stable up to temperatures of 950 °C in an oxygen-rich atmosphere, after which a slow decomposition into a volatile CrO_3 occurs [49]; thus, its presence might be considered beneficial for high-temperature applications below these temperatures. Although the SPS compaction was done at a temperature of 1000 °C, the process was done in a vacuum instead of an oxygen-rich atmosphere, so the distribution of Cr_2O_3 was within the interior of the alloy, which sufficiently preserved the oxides.

The previously mentioned results of the MA+SPS alloys at different temperatures are superior to those reported by Jiang et al. [30], who prepared an ultrafine-grained $CoCrFeNiNb_{0.45}$ alloy that reached at 700 °C a UCS value of 1082 MPa due to intensive microstructural coarsening.

Furthermore, the same author also observed a further decrease in the mechanical properties (YCS of ≈ 250 MPa) when tested at 1000 °C. The investigated MA+SPS alloy might also outperform the recently developed γ'-enhanced high-entropy $Ni_{45-x}(FeCoCr)_{40}(AlTi)_{15}Hf_x$ superalloy that reached a UCS of 1569 MPa at 750 °C [33]. This presumption needs to be tested, although the preliminary results showed a highly promising 5.4% decrease in the UCS values from 2412 MPa to 2284 MPa when the MA+SPS alloy was tested at 25 °C and 600 °C.

Considering the abovementioned facts, the MA+SPS equiatomic CoCrFeNiNb alloy outperformed the as-cast counterpart for all the mechanical properties due to a combination of several aspects. First, the microstructure was significantly refined during the MA, although a certain coarsening was observed when compacted via SPS at 1000 °C. Thus, the main strengthening mechanism found in the MA+SPS equiatomic CoCrFeNiNb alloy can be attributed to grain boundary strengthening, solid solution strengthening (due to the presence of considerably larger Nb atoms compared to the rest of elements) and strengthening by a high volume fraction of homogeneously dispersed Laves phases, while excellent thermal stability was achieved partially due to sluggish diffusion of elements as well by Cr_2O_3 nanocrystalline particles that might effectively supress grain growth.

3.5 Microstructure strengthening mechanism

The strengthening model presented here aims to include all the meaningful microstructure strengthening factors that contribute to the compressive yield strength. In the case of the 8 h MA + SPS 1000 °C condition, the compression tests were able to obtain the alloy yield compression strength (YCS) only at T = 600 °C. At room temperature, the compression tests gave an estimation of the ultimate strength (UCS). Tab. 4 shows that the UCS from room temperature to 600 °C was reduced by only ~5%. It can thus be assumed that the corresponding YCS would reduce by the same rate. According to the YCS value reported in Tab. 4 and referring to the compression test at T = 600 °C, for the present model, the room-temperature YCS was assumed to be $2412 \cdot 0.95 = 2291$ MPa.

The different microstructure strengthening contributions came from the three alloy constituents, i.e., the γ phase, the Laves phases, and the Cr_2O_3 oxides. In particular, the γ

phase also experiences solid solution strengthening of some elements by twinning, tangled dislocations, and existing secondary phase particles. Other than these contributions, the pure metal strengthening of the lattice was also taken into account, and this was estimated as the pure cobalt $\sigma_0 \cong$ 255 MPa [50].

The overall microstructure strengthening was evaluated by the rule of mixtures of the different contributors. Eq. (1) was formulated and applied [51]:

$$\sigma_{CoCrFeNiNb\ HEA} = \sigma_0 + \Big[V_v^{\gamma}\big(\Delta\sigma_{Hall-Petch}^{\gamma} + \Delta\sigma_{solid-solution}^{\gamma} + \Delta\sigma_{dislocation}^{\gamma} + \Delta\sigma_{Twin\ Boundary}^{\gamma} + \Delta\sigma_{spp}^{\gamma}\big)^2 + V_v^{Laves}\big(\Delta\sigma_{Hall-Petch}^{Laves} + \Delta\sigma_{Thermal\ Exp.}^{Laves}\big)^2 + V_v^{Cr2O3}\big(+\Delta\sigma_{LT}^{Cr2O3} + \Delta\sigma_{Thermal\ Exp.}^{Cr2O3}\big)^2\Big]^{0.5}$$

Eq. (1)

The individual microstructure terms were calculated as follows. The volume fractions of the three phases, namely V_v^{γ}, V_v^{Laves}, and V_v^{Cr2O3}, were determined by stereological means (EN-112) using 15 different TEM micrographs. These data are reported in

Tab. 5.

The solid solution strengthening acting within the γ phase can be considered of particular importance. The role of the solute elements in HEAs is primarily attributed to atomic size differences among the solute atoms and the elements constituting the bulk of the existing phases [52, 53]. The TEM inspections, SAEDPs (Fig. 8), EDS analyses (Fig. 7 and Tab. 3), and XRD (Fig. 5) showed that the γ phase is composed of FCC Co with Cr, Fe, Ni, and Nb solute atoms. The Laves phase is constituted by a HCP $(Co,Fe,Ni)_2(Cr,Nb)$ phase with minimal solute atoms within the phase. The solute element strengthening contribution is therefore included only for the γ phase. The atomic radii (Å) of the elements that constituted the HEA are Co (1.26), Cr (1.66), Fe (1.27), Ni (1.25), and Nb (1.98). According to [53] and references therein, the solute strengthening contribution essentially comes from those elements having a significant atomic size difference with respect to the cobalt. Ni and Fe have an atomic radius essentially the same as Co, while Cr and Nb are the two elements that have atomic radii that significantly differ from the Co atomic radius. These two elements account for a solid-solution γ matrix strengthening of ~65 MPa for Cr and ~120 MPa for Nb, yielding a total γ matrix solid-solution strengthening $\Delta\sigma^{\gamma}_{solid\text{-}solution} \cong 185$ MPa.

The tangled dislocation strengthening value was calculated using the well-known Eq. (2):

$$\Delta\sigma^{\gamma}_{dislocation} = M\alpha Gb(\rho_{dislocation}^{0.5}) \qquad \text{Eq. (2)}$$

Here, for the FCC γ phase, $M = 3.06$, $\alpha = 0.2$ [54], and the Co Burger's vector is $b = 0.255$ nm. The shear modulus G was assumed to be the same as the equiatomic CoCrFeNiMn HEA and thus was set to 74 GPa [55]. The tangled dislocation density within the γ phase was measured with a stereological method by counting dislocation ends that intercepted equal radius circles in 15 different TEM micrographs and for more than 50 γ grains. The tangled dislocation distribution within the γ grains was revealed by tilting the sample to align the beam to the γ [111] zone axis. The mean dislocation density, $\rho_{dislocation}$, is reported in

Tab. 5, and the related statistical data are shown in a plot in Fig. 13. The dislocation strengthening calculated by Eq. (2) was $\Delta\sigma^{\gamma}_{dislocation}$ = 310 $\pm$ 20 MPa.

According to a previous study [56-58], the contribution from the twin boundaries, $\Delta\sigma^{\gamma}_{Twin\ Boundary}$, was calculated by a Hall-Petch type relationship as follows, Eq. (3):

$$\Delta\sigma^{\gamma}_{Twin\ Boundary} = K_{TB}(\lambda_{TB})^{-0.5} \quad \text{Eq. (3)}$$

where K_{TB} is a Hall-Petch type constant equivalent to $K^{nc\text{-}\gamma}_{HP}$ and λ_{TB} is the average twin boundary (TB) spacing. The $K^{nc\text{-}\gamma}_{HP}$ = 0.035 MPa·m$^{1/2}$, as reported in [58]. The TB spacing was statistically evaluated with 20 high-magnification TEM micrographs that contained more than 100 individual γ grains and whose distribution is shown in a plot in Fig. 13. The related mean value is reported in

Tab. 5. The mean twin strengthening contribution is thus $\Delta\sigma^{\gamma}_{Twin\ Boundary}$ = 340 ± 40 MPa.

The contribution from the grain boundaries, i.e., Hall-Petch strengthening, was determined for both the γ phase and the Laves phase. The Hall-Petch relationship used constant K_{HP}, in which the nanometric nature of both phases (100-200 nm in equivalent diameter) was used, as shown in Eqs. (4a) and (4b):

$$\Delta\sigma^{\gamma}_{Hall\text{-}Petch} = K^{\gamma}_{HP}(d_{\gamma})^{-0.5} \text{ and } \Delta\sigma^{Laves}_{Hall\text{-}Petch} = K^{Laves}_{HP}(d_{Laves})^{-0.5} \quad \text{Eqs. (4a), (4b)}$$

where K^{γ}_{HP} and K^{Laves}_{HP} are the Hall-Petch constants for nanocrystalline grains d_{γ} and the Laves phase d_{Laves}, respectively, which are known to be significantly smaller than the values generally used for the coarse-grained counterparts (typically micrometre-scale grains). In this regard, several studies have shown that some physical and mechanical parameters of CoCrFeNiNb, CoCrFeNiMn, and other Co-based HEAs are similar to those of micrometre, submicrometre, and even nanocrystalline pure Fe [53, 59-61]. Thus, the two Hall-Petch constants K^{γ}_{HP} and K^{Laves}_{HP} were set to 0.35 MPa·m$^{-1/2}$. The two mean equivalent diameters of the γ phase grains and Laves phase grains, d_{γ} and d_{Laves}, were statistically evaluated from 15 different TEM micrographs and contained more than 400 counts per phase. The size distribution is shown in Fig. 13, and the related mean equivalent diameters are reported in

Tab. 5. Therefore, the mean Hall-Petch strengthening contribution from the γ phase is $\Delta\sigma^{\gamma}_{Hall\text{-}Petch}$ = 830 $\pm$ 90 MPa, and that from the Laves phase is $\Delta\sigma^{Laves}_{Hall\text{-}Petch}$ = 1010 $\pm$ 80 MPa.

The γ phase was also strengthened by the existing secondary phase particles that were detected by TEM. These were quite small and round-shaped, with mean equivalent diameter, d_{spp} = 7.5 $\pm$ 0.5 nm, a mean spacing, λ = 23 $\pm$ 3 nm, and a volume fraction, V_v^{spp} = 1.2 $\pm$ 0.2% of the $V_v^{\gamma\ phase}$. Based on well-established models of strengthening from secondary phase particles ([51] and references therein), it can be assumed that the secondary phase particles have a mean diameter corresponding to a typical dislocation strengthening mechanism of bowing, which, according to [51, 62, 63], can be calculated by Eq. (5):

$$\Delta\sigma_{spp} = \frac{KM}{(1-\nu)^{0.5}} \frac{Gb}{(\lambda_{spp}-d_{spp})} \quad \text{Eq. (5)}$$

where K = 0.127 and Poisson's ratio ν = 0.31. The secondary phase particle strengthening contribution was thus calculated as $\Delta\sigma_{spp}$ = 570 $\pm$ 110 MPa.

A further strengthening contribution came from the Cr_2O_3 oxides that were located at the grain boundaries and the triple junctions of the γ/Laves alloy structure. This strengthening contribution is typically considered to be a composite-like mechanism.

The Cr_2O_3 oxides have a spherical morphology and a mean dimension that fit the typical strengthening mechanism of composite particles in metal matrix composites. The marked difference occurred in their distribution and location because the Cr_2O_3 oxides only occurred at the γ/γ, γ/Laves, or Laves/Laves grain boundaries, and at the boundary triple joints. With this said, it is possible to apply a typical strengthening model used to calculate the microstructure strengthening contribution of the composite particles. In this respect, according to the shear-lag model proposed by Nardone and Prewo in [64], the Cr_2O_3 oxides reinforced the alloy by carrying a fraction of the load (load-transfer strengthening contribution, σ_{LT}) from the matrix, i.e., from the γ and Laves phases.

This strengthening contribution strongly depends on the morphology of the particles, namely, on their aspect ratio [61, 62, 64] as shown in Eq. (6a):

$$\Delta\sigma_{LT}^{Cr2O3} = \sigma_0 \left(1 + \frac{A(L+t)}{4L}\right) V_v^{Cr2O3} + \sigma_0 (1 - V_v^{Cr2O3}) \quad \text{Eq. (6a)}$$

where σ_0 is the Co matrix stress, which in this case is the HEA $\sigma_0 \cong 255$ MPa; V_v^{Cr2O3} *is* the Cr_2O_3 oxide volume fraction; *L* is the particle size facing the load direction; *t is* the mean particle thickness; and *A = L/t is* the particle aspect ratio. For equiaxed particles, as in the present case, Eq. (6a) reduces to Eq. (6b):

$$\Delta\sigma_{LT}^{Cr2O3} = \sigma_{LT} - \sigma_0 = 0.5V_v^{Cr2O3}\sigma_0 \quad \text{Eq. (6b)}$$

The Cr_2O_3 volume fraction, V_v^{Cr2O3}, was estimated to be $3 \pm 1\%$, and thus, the corresponding strengthening contribution was $\Delta\sigma_{LT}^{Cr2O3} = 4 \pm 1$ MPa.

In general, the presence of sub-micrometre and micrometre particles also generates a microstructure mismatch due to the different thermal expansion coefficients (CTE) between the particles and the matrix. This, in turn, induces a dislocation density rise, yielding an additional strengthening contribution to the alloy, generally named the particle thermal expansion contribution, $\Delta\sigma_{Thermal\ Exp.}^{Cr2O3}$ [62, 64]. In fact, the relatively large thermal expansion coefficient difference between the matrix and the Cr_2O_3 oxides during the high-temperature compaction processes creates a misfit strain among the Cr_2O_3 oxides and the γ phase and Laves phase grain boundaries. This also holds for the Laves phases that have a geometric morphology that is more similar to a parallelogram than a sphere, as in the case of the Cr_2O_3 oxides. The additional strengthening from the Cr_2O_3 oxides and Laves phase, $\Delta\sigma_{Thermal\ Exp.}^{Laves}$, was calculated by Eq. (7) [64]:

$$\Delta\sigma_{Thermal\ Exp.}^{Cr2O3} = \alpha\mu Gb(\rho_{Cr2O3\_thermal}^{0.5}) \quad \text{Eq. (7a)}$$

$$\Delta\sigma_{Thermal\ Exp.}^{Laves} = \alpha\mu Gb(\rho_{Laves\_thermal}^{0.5}) \quad \text{Eq. (7b)}$$

This additional dislocation strengthening mechanism induced by the presence of the grain boundary Cr_2O_3 oxides and the Laves phase is strongly dependent on the particle geometry and specifically dependent on the particle surface-to-volume ratio (S/V). In the case of the spherical Cr_2O_3 oxides, $S/V = 6/d_{Cr2O3} = 8.6 \cdot 10^{-2}$ nm^{-1}. For the Laves phase, their parallelogram-like morphology was assumed to be essentially cubic. Thus, according to the specific zone axis selected for the TEM inspections (HCP [1-100] and [11-20] Laves zone axes), the quasi-cubic-like Laves phase had side $s = d_{Laves} \cdot \sqrt{2}$ and $S/V = 6/s = 7.1 \cdot 10^{-2}$ nm^{-1}. The calculated S/V ratio of

the intergranular Cr_2O_3 oxide particles was ~17% larger than that of the intergranular Laves phase particles. Therefore, according to Eq. (7a) and (7b), the two thermal expansion strengthening terms were $\Delta\sigma_{Thermal\ Exp.}^{Cr2O3}$ = 280 $\pm$ 60 MPa and $\Delta\sigma_{Thermal\ Exp.}^{Laves}$ = 330 $\pm$ 60 MPa.

The same arguments can be drawn for the strengthening factor that is likely to occur due to a geometrically mismatch in the reinforcement particles. This is usually taken into account for composite particles in metal matrix composite materials [62]. Nevertheless, in the present case, the Cr_2O_3 oxides did not exert a real geometrical mismatch because they were present as grain boundary features and were not located within the matrix, where they acted as coarse reinforcement particles.

Therefore, the strengthening contribution of the Cr_2O_3 oxides was limited to the $\Delta\sigma_{LT}$ and the $\Delta\sigma_{Thermal\ Exp.}^{Cr2O3}$, thus resulting in $\Delta\sigma_{Cr2O3} = \Delta\sigma_{LT} + \Delta\sigma_{Thermal\ Exp.}^{Cr2O3} \cong 290 \pm 60$ MPa.

Tab. 5: Experimental data used to determine the microstructure strengthening contributions for the 8 h MA+SPS alloy compacted at 1000 °C.

	γ phase	Laves	Cr_2O_3	$\Delta\sigma^{min}$ [MPa]	$\Delta\sigma^{max}$ [MPa]	**$\Delta\sigma^{mean}$ [MPa]**
V_v, %	72 ± 7	25 ± 6	3 ± 1			
$\rho_{dislocation}$, 10^{15} m^{-2}	0.70 ± 0.1	-	-	290	330	**310**
λ_{TB}, nm	11.0 ± 2.5	-	-	300	380	**340**
d_γ, nm	180 ± 45	-	-	740	940	**830**
d_{spp}, nm	7.5 ± 0.5	-	-			
λ_{spp}, nm	23 ± 3	-	-	460	680	**570**
V_v^{spp} of $V_v^{\gamma\ phase}$, %	1.4 ± 0.2	-	-			
d_{Laves}, nm	-	120 ± 20	-	940+270	1100+390	**1010+330**
d_{Cr2O3}, nm	-	-	70 ± 20	230	350	**290**

The last three columns report the minimum, the maximum, and the mean strengthening contributions determined from the experimental errors according to Eqs. (1)-(7). *(V_v - volume fraction of corresponding phase in %; $\rho_{dislocation}$ - dislocation density in 10^{15} m^{-2}; λ_{TB} - average twin boundary spacing in nm; d_γ - mean equivalent diameter of the γ grains in nm; d_{spp} - mean equivalent diameter of secondary phase particles in the γ phase in nm; λ_{spp} - mean spacing of secondary phase particles in the γ phase in nm; V_v^{spp} - volume fraction of secondary phase particles in the γ phase in %; d_{Laves} - mean equivalent diameter of the Laves grains in nm; d_{Cr2O3} - mean equivalent diameter of the Cr_2O_3 grains in nm)*

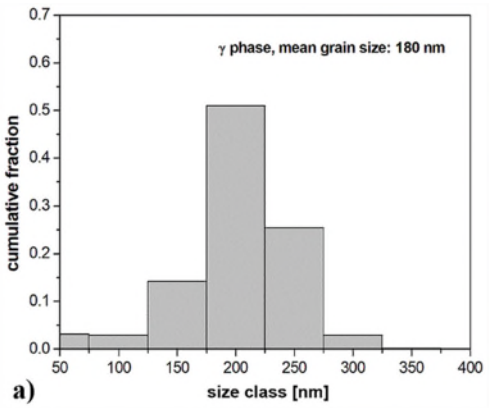

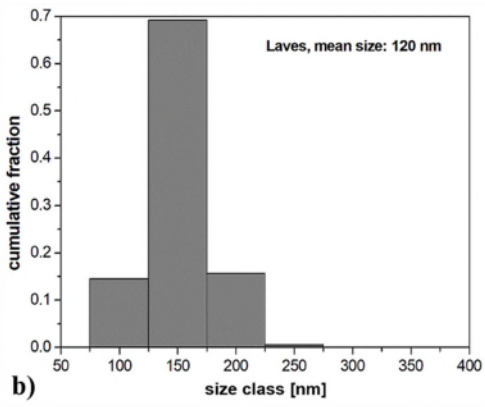

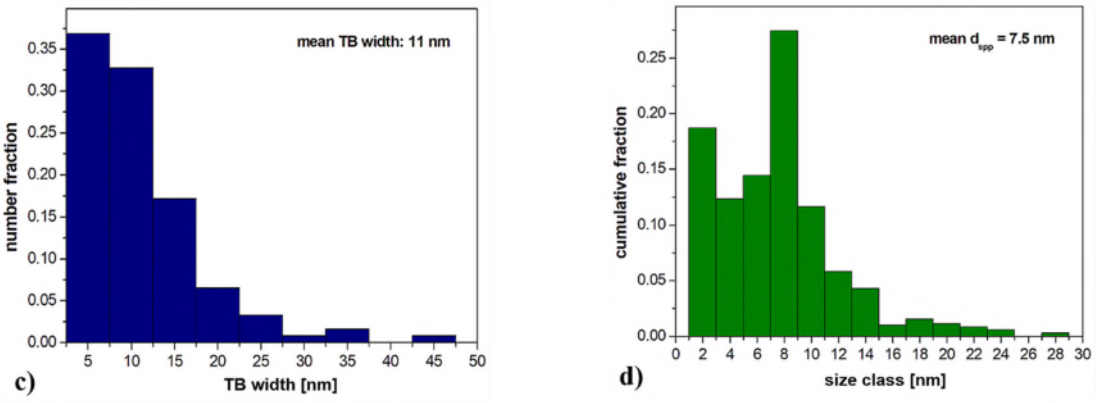

Fig. 12. Statistical evaluation of microstructure parameters used to calculate the different microstructure strengthening terms through Eqs. (1)-(7) for the 8 h MA+SPS alloy compacted at 1000 °C showing: a) grain size distribution of both γ phase, d_g^{γ} and b) Laves phase, d_g^{Laves}; c) distribution of the twin boundary spacing, λ_{TB}; d) size distribution of second-phase particles within the γ phase, d_{spp}.

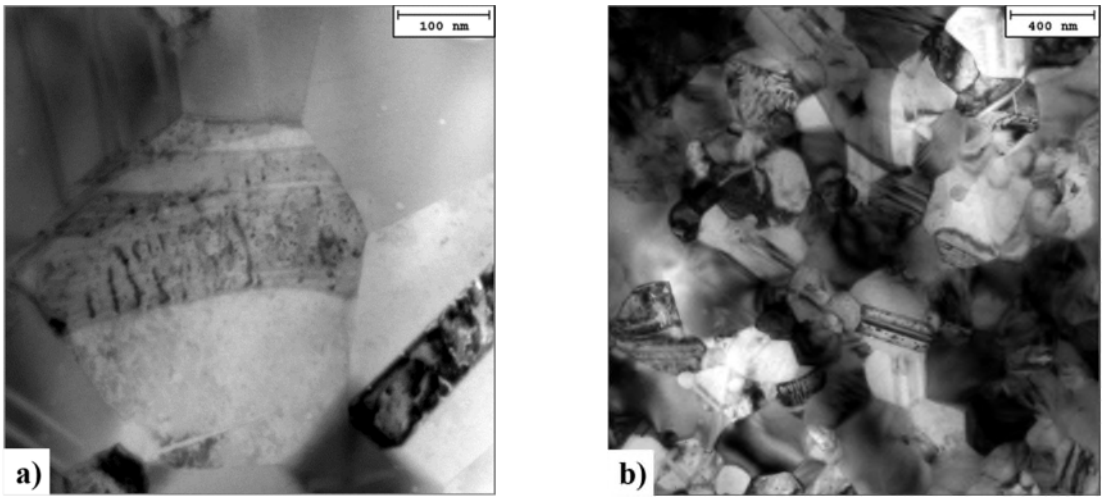

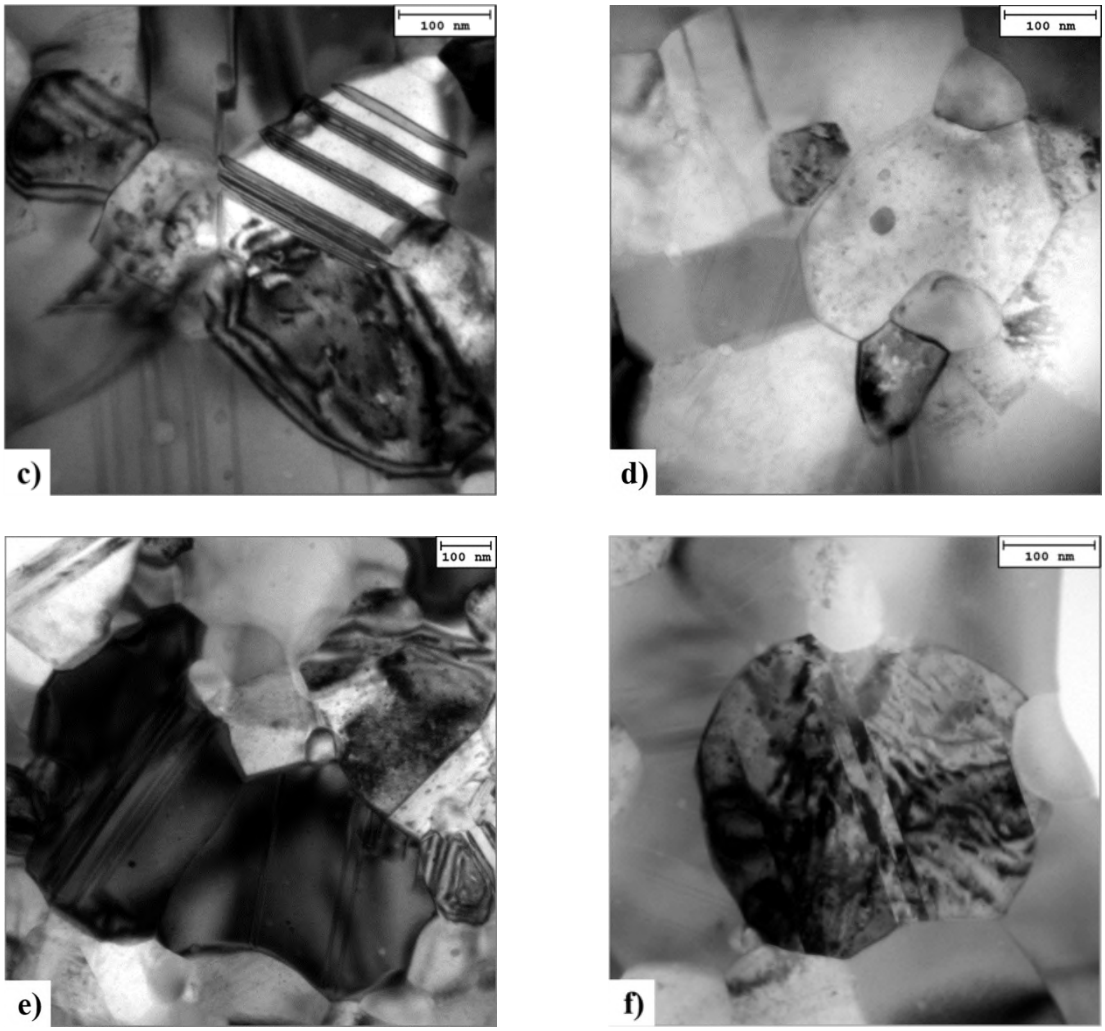

Fig. 13. BF-TEM representative micrographs showing the typical microstructure strengthening mechanisms including: a) dislocation strengthening within the γ-phase, ρ_d; b) grain size of both γ and Laves phases, d_g^{γ}, and d_g^{Laves}; c) typical twin boundary morphology and spacing, λ_{TB}, within the γ-phase; d) a representative micrograph showing the typical size of Cr_7C_3 carbides within the γ-grains; in e), typical size of the intergranular rounded Cr_2O_3; in f), BF-TEM displaying the three existing alloy constituents: γ-phase, Laves, Cr_2O_3.

In some of the γ-grains few small rounded secondary-particles were observed. These were identified as Cr_7C_3 carbides ad formed by the effect of the induced agglomeration of C-solute with Cr. This, in turns was promoted to evolve forming semi-coherent boundaries within the γ-matrix, and thus carbide particles. The driving force to promote a fraction of the solute C in Cr_7C_3 carbide particles is given by the SPS process at 1000°C. It resulted that the quite limited

fraction of these carbides and their mean size make these particles not relevant by a strengthening contribution viewpoint. Thence, the possible strengthening contribution coming for the existence of these rare carbides was not taken onto account in the strengthening model here proposed. The rather rare presence of Cr-rich carbides has been also reported by Praveen et al. [65] who also used a combination of MA and SPS for preparation of theirs CoCrFeNi alloy.

All the calculated microstructure strengthening terms were added to Eq. (1) to calculate the strengthening mechanism of the sub-micrometre-grained equiatomic CoCrFeNiNb HEA. This microstructure strengthening model was compared to the yield compression strength (YCS) at room temperature, that was derived from the experimental value of the UCS = 2412 MPa (see Table 4). According to what found by compression test at 600 °C the 8h-MA + SPS at 1000 °C HEA, the YCS was only 5% lower than the UCS. The compression curves reported in Fig. 11 seem to suggest the same relationship between UCS and YCS at the lower compression testing temperatures (400 °C and room-temperature). It was thus considered to likely be maintained the same 5% lower compression value of YCS respect to the measured UCS, that is a value of 2291 MPa. The expected experimental accuracy and calculated strengthening terms can easily considered as up to some 5%, that is, YCS = 2300 $\pm$ 100 MPa.

This resulted in the overall microstructure strengthening model, according to the rule of mixtures of Eq. (1), and yielded an alloy strength of $\sigma_{CoCrFeNiNb\ HEA}$ = 2250 $\pm$ 270 MPa. Thus, the proposed microstructure-based model fully agreed with the experimental results for the alloy compression strength at room temperature (Fig. 11). The most relevant strengthening contribution can be identified as the γ phase and related microstructure features (twinning, tangled dislocations, and secondary-phase particles). The strengthening contribution of the Laves phase was composite-type, as well as that of the few Cr_2O_3 oxides.

The microstructure model reported here and the obtained results agree well with similar proposed models and related findings that were recently published by Fu et al. in [66]. In their study, they attributed the major strengthening contributions to the yield stress to the FCC phase grain boundaries and tangled dislocations in a $Co_{25}Ni_{25}Fe_{25}Al_{7.5}Cu_{17.5}$ HEA. On the other hand, a simpler strengthening model including the solid-solution, grain boundary, secondary-phase particles, and stacking-faults (SF) strengthening terms, proposed by Zhao et al. [67], was able to account for the mechanical response of a CoCrNi medium-entropy alloy (MEA) to some

extent. In this latter case, in addition to the FCC phase grain boundary, a significant strengthening contribution was given by the SFs within the FCC phase. The key role of the SFs was also reported in two HEAs, i.e., AlCoCrCuFeNi by Ganji et al. [68] and CoCrFeMnNi by Laurent-Brocq et al. [29], although in the latter case, the role of the SFs was indirectly inferred by modelling the alloy hardness.

Similar microstructure strengthening models were proposed in other recent publications [69-72]. In particular, Tong et al. [69] identified essentially the same microstructure contributions to model the tensile stress of a non-equiatomic $FeCoNiCrTi_{0.2}$ HEA. In that study, solid solution strengthening and secondary-phase particles within FCC grains, and both coherent and anti-phase boundary energy, were considered. SF energy accounted for a significant fraction of the alloy stress, which is in good agreement with the present findings. In [70], Gao et al. recognized three major strengthening contributions in a CrMnFeCoNi HEA: FCC grain refinement (Hall-Petch), precipitation strengthening and tangled dislocations within the FCC phase. In [71], Kang et al. modelled the compressive yield stress of a WNbMoTaV HEA and identified similar strengthening contributions of the ones described here. In their work, they found that the extremely high compression yield stress of 2618 MPa was primarily from the FCC grain boundary strengthening due to the solid solution and the existing secondary-phase particle Orowan strengthening within the FCC phase. One can see that the results reported herein are in good accordance with the findings of others who dealt with similar or comparable alloy systems.

A similar model proposed by He et al. [72] identified precipitation hardening as the dominant strengthening contribution in four different FeCoNiCr-based HEAs.

The rule of mixtures and summation of the different microstructure strengthening phases that was proposed herein is in good agreement with the works by Huo et al. [73] for a CoCrFeNiTa HEA and by Stepanov et al. [74] for ($AlCr_{x=0.5/1.0/1.5}NiTiV$) different HEAs used a partitioning approach for the different phase volume fractions.

Finally, a quadratic sum of the different types of contributions was extensively justified and discussed in a previous published work by Cabibbo [50].

4. Conclusion

Equiatomic CoCrFeNiNb alloys were prepared by a combination of MA+SPS and compared with an as-cast counterpart. The combination of preparation techniques resulted in significant grain refinement, showing the presence of sub-micrometre grains of either an FCC solid solution (γ type-like phase) or of Laves phases strengthened by nanocrystalline Cr_2O_3 particles. The MA+SPS alloys were compacted at 800 °C or 1000 °C to compare their microstructures and mechanical properties. Although the compaction at 800 °C maintained an ultrafine-grained/nanocrystalline microstructure, which is beneficial for the mechanical properties, the residual porosity and particle-to-particle cohesion were rather poor. Therefore, the MA+SPS alloy compacted at 1000 °C was mainly investigated and showed exceptional properties, such as reaching a hardness of 798 ± 9 HV 30 and UCS of 2412 MPa. These excellent properties were achieved due to a refined microstructure that contained stacking faults and deformation nanotwins preferentially in the FCC solid solution that contributed to the strengthening of the MA+SPS alloy. The results of the compressive tests were in good agreement with the microstructure strengthening model based on quantitative TEM analyses. It was found that the highest contribution towards the strength of prepared 8 h MA+SPS alloy was caused by strengthening of the FCC solid solution (γ type-like phase) which contained a lot of microstructure features including twinning, tangled dislocations, and secondary-phase particles. The same alloy also showed exceptional thermal stability, maintaining or just lightly reducing the above-mentioned properties when tested after long-term annealing at laboratory temperature or at 600 °C. That was primarily due to sluggish diffusion, although the presence of a small volume fraction of thermally stable Cr_2O_3 nanocrystalline particles might also partially hinder the grain growth. On the other hand, the as-cast alloy showed the presence of eutectic-like structures (FCC solid solution + HCP Laves phase) with primary dendrites (HCP Laves phase), whose dimensions reached tens to several hundreds of micrometres, which decreased the mechanical properties.

5. Acknowledgement

This work was supported by the specific university research (MSMT No 21-SVV/2019).

References

1. B. Cantor, I.T.H. Chang, P. Knight, and A.J.B. Vincent, Microstructural development in equiatomic multicomponent alloys, Mater. Sci. Eng., A. 375-377 (2004) 213-218. https://doi.org/10.1016/j.msea.2003.10.257
2. Y. Yu, F. He, Z. Qiao, Z. Wang, W. Liu, and J. Yang, Effects of temperature and microstructure on the triblogical properties of CoCrFeNiNbx eutectic high entropy alloys, J. Alloys Compd. 775 (2019) 1376-1385. https://doi.org/10.1016/j.jallcom.2018.10.138
3. M. Zhang, R. Li, T. Yuan, X. Feng, L. Li, S. Xie, and Q. Weng, Densification and properties of B4C-based ceramics with CrMnFeCoNi high entropy alloy as a sintering aid by spark plasma sintering, Powder Technol. 343 (2019) 58-67. https://doi.org/10.1016/j.powtec.2018.11.005
4. M. Vaidya, G.M. Muralikrishna, and B.S. Murty, High-entropy alloys by mechanical alloying: A review, J. Mater. Res. 34 (2019) 664-686. 10.1557/jmr.2019.37
5. U. Sunkari, S.R. Reddy, S. Chatterjee, and P.P. Bhattacharjee, Effect of prolonged aging on phase evolution and mechanical properties of intermetallic strengthened CoCrFeNi2.1Nbx high entropy alloys, Mater. Lett. 248 (2019) 119-122. https://doi.org/10.1016/j.matlet.2019.04.012
6. J. Joseph, N. Haghdadi, K. Shamlaye, P. Hodgson, M. Barnett, and D. Fabijanic, The sliding wear behaviour of CoCrFeMnNi and AlxCoCrFeNi high entropy alloys at elevated temperatures, Wear. 428-429 (2019) 32-44. https://doi.org/10.1016/j.wear.2019.03.002
7. X. Jin, J. Bi, L. Zhang, Y. Zhou, X. Du, Y. Liang, and B. Li, A new CrFeNi2Al eutectic high entropy alloy system with excellent mechanical properties, J. Alloys Compd. 770 (2019) 655-661. https://doi.org/10.1016/j.jallcom.2018.08.176
8. A. Munitz, S. Salhov, G. Guttmann, N. Derimow, and M. Nahmany, Heat treatment influence on the microstructure and mechanical properties of AlCrFeNiTi0.5 high entropy alloys, Mater. Sci. Eng., A. 742 (2019) 1-14. https://doi.org/10.1016/j.msea.2018.10.114
9. F. He, Z. Wang, P. Cheng, Q. Wang, J. Li, Y. Dang, J. Wang, and C.T. Liu, Designing eutectic high entropy alloys of CoCrFeNiNbx, J. Alloys Compd. 656 (2016) 284-289. https://doi.org/10.1016/j.jallcom.2015.09.153
10. W.H. Liu, J.Y. He, H.L. Huang, H. Wang, Z.P. Lu, and C.T. Liu, Effects of Nb additions on the microstructure and mechanical property of CoCrFeNi high-entropy alloys, Intermetallics. 60 (2015) 1-8. https://doi.org/10.1016/j.intermet.2015.01.004
11. Y. Zhang, X. Yang, and P.K. Liaw, Alloy Design and Properties Optimization of High-Entropy Alloys, JOM. 64 (2012) 830-838. 10.1007/s11837-012-0366-5
12. D.B. Miracle and O.N. Senkov, A critical review of high entropy alloys and related concepts, Acta Mater. 122 (2017) 448-511. https://doi.org/10.1016/j.actamat.2016.08.081

13. Y. Xie, D. Zhou, Y. Luo, T. Xia, W. Zeng, C. Li, J. Wang, J. Liang, and D. Zhang, Fabrication of CoCrFeNiMn high entropy alloy matrix composites by thermomechanical consolidation of a mechanically milled powder, Mater. Charact. 148 (2019) 307-316. https://doi.org/10.1016/j.matchar.2019.01.002
14. I. Baker, M. Wu, and Z. Wang, Eutectic/eutectoid multi-principle component alloys: A review, Mater. Charact. 147 (2019) 545-557. https://doi.org/10.1016/j.matchar.2018.07.030
15. Z. Fu, L. Jiang, J.L. Wardini, B.E. MacDonald, H. Wen, W. Xiong, D. Zhang, Y. Zhou, T.J. Rupert, W. Chen, and E.J. Lavernia, A high-entropy alloy with hierarchical nanoprecipitates and ultrahigh strength, Science Advances. 4 (2018) eaat8712. 10.1126/sciadv.aat8712
16. W. Luo, Y. Liu, Y. Luo, and M. Wu, Fabrication and characterization of WC-AlCoCrCuFeNi high-entropy alloy composites by spark plasma sintering, J. Alloys Compd. 754 (2018) 163-170. https://doi.org/10.1016/j.jallcom.2018.04.270
17. C. Sun, P. Li, S. Xi, Y. Zhou, S. Li, and X. Yang, A new type of high entropy alloy composite Fe18Ni23Co25Cr21Mo8WNb3C2 prepared by mechanical alloying and hot pressing sintering, Mater. Sci. Eng., A. 728 (2018) 144-150. https://doi.org/10.1016/j.msea.2018.05.022
18. H. Zhang, L. Zhang, X. Liu, Q. Chen, and Y. Xu, Effect of Zr Addition on the Microstructure and Mechanical Properties of CoCrFeNiMn High-Entropy Alloy Synthesized by Spark Plasma Sintering, Entropy. 20 (2018) 810.
19. F. Průša, A. Šenková, V. Kučera, J. Čapek, and D. Vojtěch, Properties of a high-strength ultrafine-grained CoCrFeNiMn high-entropy alloy prepared by short-term mechanical alloying and spark plasma sintering, Mater. Sci. Eng., A. 734 (2018) 341-352. https://doi.org/10.1016/j.msea.2018.08.014
20. R.M. Pohan, B. Gwalani, J. Lee, T. Alam, J.Y. Hwang, H.J. Ryu, R. Banerjee, and S.H. Hong, Microstructures and mechanical properties of mechanically alloyed and spark plasma sintered Al0.3CoCrFeMnNi high entropy alloy, Mater. Chem. Phys. 210 (2018) 62-70. https://doi.org/10.1016/j.matchemphys.2017.09.013
21. F. He, Z. Wang, Q. Wu, D. Chen, T. Yang, J. Li, J. Wang, C.T. Liu, and J.-j. Kai, Tuning the defects in face centered cubic high entropy alloy via temperature-dependent stacking fault energy, Scr. Mater. 155 (2018) 134-138. https://doi.org/10.1016/j.scriptamat.2018.06.002
22. J. Pan, T. Dai, T. Lu, X. Ni, J. Dai, and M. Li, Microstructure and mechanical properties of Nb25Mo25Ta25W25 and Ti8Nb23Mo23Ta23W23 high entropy alloys prepared by mechanical alloying and spark plasma sintering, Mater. Sci. Eng., A. 738 (2018) 362-366. https://doi.org/10.1016/j.msea.2018.09.089
23. S.G. Ma and Y. Zhang, Effect of Nb addition on the microstructure and properties of AlCoCrFeNi high-entropy alloy, Mater. Sci. Eng., A. 532 (2012) 480-486. https://doi.org/10.1016/j.msea.2011.10.110

24. J.B. Cheng, X.B. Liang, and B.S. Xu, Effect of Nb addition on the structure and mechanical behaviors of CoCrCuFeNi high-entropy alloy coatings, Surf. Coat. Technol. 240 (2014) 184-190. https://doi.org/10.1016/j.surfcoat.2013.12.053
25. G. Qin, S. Wang, R. Chen, X. Gong, L. Wang, Y. Su, J. Guo, and H. Fu, Microstructures and mechanical properties of Nb-alloyed CoCrCuFeNi high-entropy alloys, J. Mater. Sci. Technol. 34 (2018) 365-369. https://doi.org/10.1016/j.jmst.2017.11.007
26. H. Jiang, L. Jiang, D. Qiao, Y. Lu, T. Wang, Z. Cao, and T. Li, Effect of Niobium on Microstructure and Properties of the CoCrFeNbxNi High Entropy Alloys, J. Mater. Sci. Technol. 33 (2017) 712-717. https://doi.org/10.1016/j.jmst.2016.09.016
27. Q. Fang, Y. Chen, J. Li, Y. Liu, and Y. Liu, Microstructure and mechanical properties of FeCoCrNiNbX high-entropy alloy coatings, Phys. B. 550 (2018) 112-116. https://doi.org/10.1016/j.physb.2018.08.044
28. F. He, Z. Wang, X. Shang, C. Leng, J. Li, and J. Wang, Stability of lamellar structures in CoCrFeNiNbx eutectic high entropy alloys at elevated temperatures, Mater. Des. 104 (2016) 259-264. https://doi.org/10.1016/j.matdes.2016.05.044
29. M. Laurent-Brocq, P.A. Goujon, J. Monnier, B. Villeroy, L. Perrière, R. Pirès, and G. Garcin, Microstructure and mechanical properties of a CoCrFeMnNi high entropy alloy processed by milling and spark plasma sintering, J. Alloys Compd. 780 (2019) 856-865. https://doi.org/10.1016/j.jallcom.2018.11.181
30. H. Jiang, D. Qiao, Y. Lu, Z. Ren, Z. Cao, T. Wang, and T. Li, Direct solidification of bulk ultrafine-microstructure eutectic high-entropy alloys with outstanding thermal stability, Scr. Mater. 165 (2019) 145-149. https://doi.org/10.1016/j.scriptamat.2019.02.035
31. B. Liu, J. Wang, Y. Liu, Q. Fang, Y. Wu, S. Chen, and C.T. Liu, Microstructure and mechanical properties of equimolar FeCoCrNi high entropy alloy prepared via powder extrusion, Intermetallics. 75 (2016) 25-30. https://doi.org/10.1016/j.intermet.2016.05.006
32. F. He, D. Chen, B. Han, Q. Wu, Z. Wang, S. Wei, D. Wei, J. Wang, C.T. Liu, and J.-j. Kai, Design of D022 superlattice with superior strengthening effect in high entropy alloys, Acta Mater. 167 (2019) 275-286. https://doi.org/10.1016/j.actamat.2019.01.048
33. L. Zhang, Y. Zhou, X. Jin, X. Du, and B. Li, The microstructure and high-temperature properties of novel nano precipitation-hardened face centered cubic high-entropy superalloys, Scr. Mater. 146 (2018) 226-230. https://doi.org/10.1016/j.scriptamat.2017.12.001
34. Z.-S. Nong, Y.-N. Lei, and J.-C. Zhu, Wear and oxidation resistances of AlCrFeNiTi-based high entropy alloys, Intermetallics. 101 (2018) 144-151. https://doi.org/10.1016/j.intermet.2018.07.017
35. H. Jiang, K. Han, X. Gao, Y. Lu, Z. Cao, M.C. Gao, J.A. Hawk, and T. Li, A new strategy to design eutectic high-entropy alloys using simple mixture method, Mater. Des. 142 (2018) 101-105. https://doi.org/10.1016/j.matdes.2018.01.025

36. F. He, Z. Wang, J. Wang, Q. Wu, D. Chen, B. Han, J. Li, J. Wang, and J.J. Kai, Abnormal γ" - ε phase transformation in the CoCrFeNiNb0.25 high entropy alloy, Scr. Mater. 146 (2018) 281-285. https://doi.org/10.1016/j.scriptamat.2017.12.009
37. C. Ai, F. He, M. Guo, J. Zhou, Z. Wang, Z. Yuan, Y. Guo, Y. Liu, and L. Liu, Alloy design, micromechanical and macromechanical properties of CoCrFeNiTax eutectic high entropy alloys, J. Alloys Compd. 735 (2018) 2653-2662. https://doi.org/10.1016/j.jallcom.2017.12.015
38. M.-H. Tsai, A.-C. Fan, and H.-A. Wang, Effect of atomic size difference on the type of major intermetallic phase in arc-melted CoCrFeNiX high-entropy alloys, J. Alloys Compd. 695 (2017) 1479-1487. https://doi.org/10.1016/j.jallcom.2016.10.286
39. F. He, Z. Wang, S. Niu, Q. Wu, J. Li, J. Wang, C.T. Liu, and Y. Dang, Strengthening the CoCrFeNiNb0.25 high entropy alloy by FCC precipitate, J. Alloys Compd. 667 (2016) 53-57. https://doi.org/10.1016/j.jallcom.2016.01.153
40. M. Vaidya, A. Karati, A. Marshal, K.G. Pradeep, and B.S. Murty, Phase evolution and stability of nanocrystalline CoCrFeNi and CoCrFeMnNi high entropy alloys, J. Alloys Compd. 770 (2019) 1004-1015. https://doi.org/10.1016/j.jallcom.2018.08.200
41. H. Cheng, X. Liu, Q. Tang, W. Wang, X. Yan, and P. Dai, Microstructure and mechanical properties of FeCoCrNiMnAlx high-entropy alloys prepared by mechanical alloying and hot-pressed sintering, J. Alloys Compd. 775 (2019) 742-751. https://doi.org/10.1016/j.jallcom.2018.10.168
42. F. Alijani, M. Reihanian, and K. Gheisari, Study on phase formation in magnetic FeCoNiMnV high entropy alloy produced by mechanical alloying, J. Alloys Compd. 773 (2019) 623-630. https://doi.org/10.1016/j.jallcom.2018.09.204
43. Ł. Rogal, D. Kalita, A. Tarasek, P. Bobrowski, and F. Czerwinski, Effect of SiC nano-particles on microstructure and mechanical properties of the CoCrFeMnNi high entropy alloy, J. Alloys Compd. 708 (2017) 344-352. https://doi.org/10.1016/j.jallcom.2017.02.274
44. S.H. Joo, H. Kato, M.J. Jang, J. Moon, E.B. Kim, S.J. Hong, and H.S. Kim, Structure and properties of ultrafine-grained CoCrFeMnNi high-entropy alloys produced by mechanical alloying and spark plasma sintering, J. Alloys Compd. 698 (2017) 591-604. https://doi.org/10.1016/j.jallcom.2016.12.010
45. W. Ji, W. Wang, H. Wang, J. Zhang, Y. Wang, F. Zhang, and Z. Fu, Alloying behavior and novel properties of CoCrFeNiMn high-entropy alloy fabricated by mechanical alloying and spark plasma sintering, Intermetallics. 56 (2015) 24-27. https://doi.org/10.1016/j.intermet.2014.08.008
46. C. Wang, W. Ji, and Z. Fu, Mechanical alloying and spark plasma sintering of CoCrFeNiMnAl high-entropy alloy, Adv. Powder Technol. 25 (2014) 1334-1338. https://doi.org/10.1016/j.apt.2014.03.014

47. W. Ji, Z. Fu, W. Wang, H. Wang, J. Zhang, Y. Wang, and F. Zhang, Mechanical alloying synthesis and spark plasma sintering consolidation of CoCrFeNiAl high-entropy alloy, J. Alloys Compd. 589 (2014) 61-66. https://doi.org/10.1016/j.jallcom.2013.11.146
48. W.H. Liu, T. Yang, and C.T. Liu, Precipitation hardening in CoCrFeNi-based high entropy alloys, Mater. Chem. Phys. 210 (2018) 2-11. https://doi.org/10.1016/j.matchemphys.2017.07.037
49. T.-G. Wang, Y. Liu, H. Sina, C. Shi, S. Iyengar, S. Melin, and K.H. Kim, High-temperature thermal stability of nanocrystalline Cr2O3 films deposited on silicon wafers by arc ion plating, Surf. Coat. Technol. 228 (2013) 140-147. https://doi.org/10.1016/j.surfcoat.2013.04.020
50. A.I.H. Committee, Properties and Selection: Nonferrous Alloys and Special- Purpose Materials, 1990.
51. M. Cabibbo, Microstructure strengthening mechanisms in different equal channel angular pressed aluminum alloys, Mater. Sci. Eng., A. 560 (2013) 413-432. https://doi.org/10.1016/j.msea.2012.09.086
52. F. Otto, A. Dlouhý, C. Somsen, H. Bei, G. Eggeler, and E.P. George, The influences of temperature and microstructure on the tensile properties of a CoCrFeMnNi high-entropy alloy, Acta Mater. 61 (2013) 5743-5755. https://doi.org/10.1016/j.actamat.2013.06.018
53. J.Y. He, W.H. Liu, H. Wang, Y. Wu, X.J. Liu, T.G. Nieh, and Z.P. Lu, Effects of Al addition on structural evolution and tensile properties of the FeCoNiCrMn high-entropy alloy system, Acta Mater. 62 (2014) 105-113. https://doi.org/10.1016/j.actamat.2013.09.037
54. T.H. Courtney, Mechanical Behavior of Materials: Second Edition, 2005.
55. E.V. Kozlov, A.N. Zhdanov, and N. Koneva, Barrier Retardation of Dislocations. Hall-Petch Problem, 2006.
56. H. Wen, T.D. Topping, D. Isheim, D.N. Seidman, and E.J. Lavernia, Strengthening mechanisms in a high-strength bulk nanostructured Cu–Zn–Al alloy processed via cryomilling and spark plasma sintering, Acta Mater. 61 (2013) 2769-2782. https://doi.org/10.1016/j.actamat.2012.09.036
57. X.H. Chen, L. Lu, and K. Lu, Grain size dependence of tensile properties in ultrafine-grained Cu with nanoscale twins, Scr. Mater. 64 (2011) 311-314. https://doi.org/10.1016/j.scriptamat.2010.10.015
58. X. Li, Y. Wei, L. Lu, K. Lu, and H. Gao, Dislocation nucleation governed softening and maximum strength in nano-twinned metals, Nature. 464 (2010) 877. 10.1038/nature08929
https://www.nature.com/articles/nature08929#supplementary-information
59. S. Guo, C. Ng, J. Lu, and C.T. Liu, Effect of valence electron concentration on stability of fcc or bcc phase in high entropy alloys, J. Appl. Phys. 109 (2011) 103505. 10.1063/1.3587228

60. C. Zhu, Z.P. Lu, and T.G. Nieh, Incipient plasticity and dislocation nucleation of FeCoCrNiMn high-entropy alloy, Acta Mater. 61 (2013) 2993-3001. https://doi.org/10.1016/j.actamat.2013.01.059
61. K.T. Ramesh, Nanomaterials: Mechanics and Mechanisms, 2009.
62. M. Cabibbo and S. Spigarelli, A TEM quantitative evaluation of strengthening in an Mg–RE alloy reinforced with SiC, Mater. Charact. 62 (2011) 959-969. https://doi.org/10.1016/j.matchar.2011.04.011
63. A.J. Kulkarni, K. Krishnamurthy, S.P. Deshmukh, and R.S. Mishra, Effect of particle size distribution on strength of precipitation-hardened alloys, J. Mater. Res. 19 (2004) 2765-2773. 10.1557/JMR.2004.0364
64. V.C. Nardone and K.M. Prewo, On the strength of discontinuous silicon carbide reinforced aluminum composites, Scr. Metall. 20 (1986) 43-48. https://doi.org/10.1016/0036-9748(86)90210-3
65. S. Praveen, J. Basu, S. Kashyap, and R.S. Kottada, Exceptional resistance to grain growth in nanocrystalline CoCrFeNi high entropy alloy at high homologous temperatures, J. Alloys Compd. 662 (2016) 361-367. https://doi.org/10.1016/j.jallcom.2015.12.020
66. Z. Fu, W. Chen, H. Wen, D. Zhang, Z. Chen, B. Zheng, Y. Zhou, and E.J. Lavernia, Microstructure and strengthening mechanisms in an FCC structured single-phase nanocrystalline Co25Ni25Fe25Al7.5Cu17.5 high-entropy alloy, Acta Mater. 107 (2016) 59-71. https://doi.org/10.1016/j.actamat.2016.01.050
67. Y.L. Zhao, T. Yang, Y. Tong, J. Wang, J.H. Luan, Z.B. Jiao, D. Chen, Y. Yang, A. Hu, C.T. Liu, and J.J. Kai, Heterogeneous precipitation behavior and stacking-fault-mediated deformation in a CoCrNi-based medium-entropy alloy, Acta Mater. 138 (2017) 72-82. https://doi.org/10.1016/j.actamat.2017.07.029
68. R.S. Ganji, P. Sai Karthik, K. Bhanu Sankara Rao, and K.V. Rajulapati, Strengthening mechanisms in equiatomic ultrafine grained AlCoCrCuFeNi high-entropy alloy studied by micro- and nanoindentation methods, Acta Mater. 125 (2017) 58-68. https://doi.org/10.1016/j.actamat.2016.11.046
69. Y. Tong, D. Chen, B. Han, J. Wang, R. Feng, T. Yang, C. Zhao, Y.L. Zhao, W. Guo, Y. Shimizu, C.T. Liu, P.K. Liaw, K. Inoue, Y. Nagai, A. Hu, and J.J. Kai, Outstanding tensile properties of a precipitation-strengthened FeCoNiCrTi0.2 high-entropy alloy at room and cryogenic temperatures, Acta Mater. 165 (2019) 228-240. https://doi.org/10.1016/j.actamat.2018.11.049
70. N. Gao, D.H. Lu, Y.Y. Zhao, X.W. Liu, G.H. Liu, Y. Wu, G. Liu, Z.T. Fan, Z.P. Lu, and E.P. George, Strengthening of a CrMnFeCoNi high-entropy alloy by carbide precipitation, J. Alloys Compd. 792 (2019) 1028-1035. https://doi.org/10.1016/j.jallcom.2019.04.121
71. B. Kang, J. Lee, H.J. Ryu, and S.H. Hong, Ultra-high strength WNbMoTaV high-entropy alloys with fine grain structure fabricated by powder metallurgical process, Mater. Sci. Eng., A. 712 (2018) 616-624. https://doi.org/10.1016/j.msea.2017.12.021

72. J.Y. He, H. Wang, H.L. Huang, X.D. Xu, M.W. Chen, Y. Wu, X.J. Liu, T.G. Nieh, K. An, and Z.P. Lu, A precipitation-hardened high-entropy alloy with outstanding tensile properties, Acta Mater. 102 (2016) 187-196. https://doi.org/10.1016/j.actamat.2015.08.076
73. W. Huo, H. Zhou, F. Fang, X. Zhou, Z. Xie, and J. Jiang, Microstructure and properties of novel CoCrFeNiTax eutectic high-entropy alloys, J. Alloys Compd. 735 (2018) 897-904. https://doi.org/10.1016/j.jallcom.2017.11.075
74. N.D. Stepanov, N.Y. Yurchenko, D.V. Skibin, M.A. Tikhonovsky, and G.A. Salishchev, Structure and mechanical properties of the AlCrxNbTiV (x = 0, 0.5, 1, 1.5) high entropy alloys, J. Alloys Compd. 652 (2015) 266-280. https://doi.org/10.1016/j.jallcom.2015.08.224

.